Politecnico di Torino

Master's Degree in Biomedical Engineering

Academic year 2023/2024

Master's Degree Thesis

"Monitoring the response to radiotherapy in cancerous skin lesions: a quantitative analysis of vascular changes using OCTA"

Supervisors:

Prof. Kristen MEIBURGER

Prof. Mengyang LIU

Ing. Giulia ROTUNNO

Candidate:

Flavia LO BUE

Abstract

Skin cancer represents the most prevalent form of malignancy worldwide, primarily categorized into cutaneous carcinomas—basal cell carcinoma and squamous cell carcinoma—and melanomas. Among the treatments for cutaneous carcinoma, radiotherapy is considered an effective option, particularly kilovolt radiotherapy. Superficial kV-based radiotherapy uses low-energy X-rays, depositing most energy in the first few millimeters of tissue. This makes it suitable for treating superficial lesions, minimizing damage to underlying tissues and enhancing treatment precision. Angiographic optical coherence tomography (OCTA) is employed to monitor treatment response. This non-invasive technique enables volumetric rendering of the tissue's vascular network without contrast agents. OCTA provides insights into tissue morphology and vascular structure, with an imaging depth of up to 1 mm, facilitating detailed visualization of epidermal and dermal microstructures. This is key for lesion analysis, as changes in vascularization can indicate angiogenesis related to tumor growth, providing important information on therapy effectiveness.

The primary goal of this thesis is to assess skin superficial lesions at three distinct time points: before radiotherapy, one month after, and three months post-treatment. The quantitative analysis of vascular network parameters aims to identify significant variations between these time points and correlate them with treatment response and effects on skin tissue.

The study involves five patients with a total of nine lesions, analyzing 22 volumes overall—12 lesion volumes and 10 volumes of healthy skin. The image processing pipeline includes preprocessing the raw data into OCT matrices, applying an intensity-based method for OCTA reconstruction, and performing artifact removal. Emphasis is placed on deep color coding and semi-automatic volume segmentation with Amira software. The vascular parameters extracted through the skeletonization of the segmented volume include vascular density, vessel radius, distance metric, sum of angles metric, number of trees, number of branches, and inflection count metric.
The results focus on the trends of extracted parameters for each lesion of each patient across three acquisition sessions. Maximum and average values of the parameters are

computed across the patients at the different time points to observe changes over time. This approach facilitates comparisons among the three sessions, highlighting any statistically significant differences. The results indicate significant changes in some of the analyzed parameters, such as vascular density vessel radius, distance metric, number of branches and inflection count metric, suggesting an evolution of the skin lesions during time. Additionally, comparing the extracted vascular parameters of healthy skin and each patient's lesions reveals that the vascular network is crucial for distinguishing healthy from diseased skin.

Finally, this thesis highlights the possibility of performing therapeutic follow-up non-invasively through the use of OCTA, presenting a significant opportunity for future development. However, limitations include the possibility that some lesions may not show significant improvements in vascular parameters due to acquisition artifacts and inaccuracies in positioning across sessions. Additionally, post-radiotherapy tissue inflammation may elicit immune responses that can affect metrics and delay observable treatment effects.

Table of Contents

1. Introduction

1.1 Skin cancer: pathogenetic processes and risk factors

The skin, as the body's largest organ, comprises three main layers: the epidermis, dermis, and subcutaneous tissue, each with distinct structures and functions (Fig 1.1).

The epidermis, the outermost layer, is ectodermal in origin and serves as a protective barrier against pathogens, chemicals, and UV radiation. It is primarily composed of keratinocytes, which form in the basal layer and differentiate as they migrate towards the surface, becoming corneocytes in the stratum corneum. The epidermis also contains melanocytes, which produce melanin, a pigment that helps protect against UV damage, and Langerhans cells, which play a role in the immune response. Being entirely epithelial, the epidermis is not vascularized and its nourishment depends on the diffusion of oxygen and nutrients from the underlying dermis.

The dermis, of mesodermal origin, supports skin structures like hair follicles, glands, and blood vessels, and houses immune cells and fibroblasts.

The subcutaneous tissue provides thermal insulation, energy storage, and mechanical protection [2].

Skin cancers are the most common type of cancer worldwide and are primarily divided into two categories: non-melanoma skin cancers (NMSC), which include basal cell carcinoma (BCC) and squamous cell carcinoma (SCC), and melanoma (CM) [3, 4, 5].

Basal cell carcinoma (BCC) originates from the basal cells located in the lower layer of the epidermis and is the most common type of skin cancer. Although BCC grows slowly and rarely metastasizes, some histological forms can exhibit locally invasive behavior. While it is not often fatal, BCC can cause significant damage and deformities to the surrounding tissues if treatment is delayed or inadequate. This invasive potential increases the risk of recurrence and often requires more extensive surgical procedures to ensure complete removal. Clinically, BCC typically appears as pearly papules that are flesh-colored or pink,

often with ulcers or visible blood vessels. Although it usually starts as a small papule that grows slowly, it typically evolves into a shiny lesion with pearly borders, prominent blood vessels, and a central ulcer. BCC typically does not have precursor lesions. It is most commonly found on the head and neck but can also develop on the trunk and limbs [3,6-7].

Squamous cell carcinoma (SCC) originates from the uncontrolled proliferation of keratinocytes in the epidermis. Compared to BCC, SCC generally grows more quickly and has a higher likelihood of metastasis, with the overall metastatic rate estimated to be between 3% and 10%, depending on factors such as tumor location, underlying medical conditions, cell differentiation, and size [7]. SCC can develop not only from direct exposure to risk factors such as UV radiation, but also in chronic wounds, scars, or pre-existing skin lesions. It can arise from certain precancerous conditions, such as actinic keratosis (scaly spots on sun-damaged skin), SCC in situ (an early form of cancer confined to the upper layers of the epidermis), Bowen's disease (a type of intraepidermal SCC that does not invade the underlying tissues), and bowenoid papulosis (a precancerous condition characterized by small papules). Actinic keratosis (AK) is a significant precancerous condition that can precede the development of squamous cell carcinoma (SCC). AK commonly occurs on sun-exposed areas of the skin and presents as rough, scaly patches that may initially go unnoticed. Research estimates that around 60% of individuals over the age of 40 who are regularly exposed to UV radiation will develop at least one AK. If left untreated, AK lesions carry the risk of progressing to SCC, with studies indicating that between 25% and 60% of SCC cases originate from AK. Identifying and managing AK is crucial in preventing its potential progression to invasive SCC. The presence of AK highlights the cumulative damage caused by UV exposure and serves as an early indicator of skin vulnerability to malignancy [7-8]. Clinically, SCC can manifest in various forms, but any lesion that does not heal on sun-exposed areas should be considered suspicious. The lesion may begin as a red papule or patch with a scaly or rough surface, and later become nodular with a wart-like or plaque-like appearance. It can be smooth, have a dry, hard surface (like a crust), or be erosive, and may bleed easily. Over time, the lesion can ulcerate and invade the underlying tissues. In some cases, it may be located below the level of the surrounding skin [7].

The cutaneous melanoma (CM) originates from melanocytes, the cells responsible for producing melanin in the epidermis.

The pathogenesis of skin cancers is complex and multifactorial, resulting from the interaction of genetic and environmental factors.

One of the primary risk factors is exposure to ultraviolet (UV) radiation, which is divided into UV-A (320–400 nm) and UV-B (290–320 nm). These rays act in different but complementary ways to damage the skin and promote the formation of skin cancers. UV-B rays are considered the main cause of skin damage, as they penetrate the outer layers of the epidermis and cause direct mutations in the DNA of keratinocytes, which can lead to cancer. UV-A rays, although penetrating deeper into the skin, do not directly damage DNA like UV-B rays, but instead act as cancer promoters, stimulating molecules that enhance tumor cell growth and weakening the skin's immune system.Additionally, another significant risk factor is skin phototype, which classifies skin based on its response to UV radiation and melanin production. People with lighter phototypes, who produce lower amounts of eumelanin, are particularly vulnerable to UV damage. This is because their skin is less protected from solar radiation, allowing UV rays to penetrate more easily, which increases the risk of accumulating mutations over time. Specifically, those with fair skin have a significantly higher risk of developing skin cancers.[3,5,6,8]

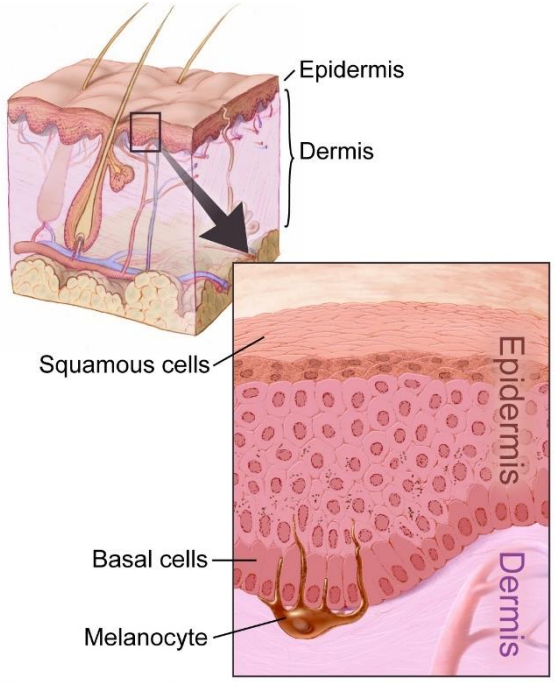

Figure 1.1 : Normal anatomy of the skin. (Source:[1]).

1.1.1 Epidemiological data

Epidemiological data on skin cancers show that BCC is the most common skin cancer worldwide, with rising incidence rates. This trend is linked not only to environmental and behavioral factors, such as prolonged UV exposure, but also to increased public awareness and advances in early diagnosis techniques. Men generally have a higher incidence of BCC compared to women, with the risk being particularly high in regions with intense UV exposure, such as those located at extreme latitudes. One of the main risk factors for developing BCC is a previous history of skin cancers: individuals who have had a BCC are significantly more likely to develop another one compared to those who have never had non-melanoma skin cancers [6].

SCC, on the other hand, is the second most common non-melanoma skin cancer [9-10]. Generally, SCC has a favorable prognosis after treatment, with five-year survival rates exceeding 90% [11]. However, despite the relatively low mortality rate compared to the number of treated cases, cSCC still accounts for a significant number of deaths overall, due to its high incidence in the population. Risk factors for SCC include not only UV exposure, but also conditions such as immunosuppression and the presence of precancerous lesions, which can increase susceptibility to the development of the disease [9-11].

1.2 Treatments for skin cancer: focus on radiotherapy

The treatment of skin cancer depends largely on the type and stage of the malignancy.

For both BCC and SCC, the preferred treatment is surgical excision, with a careful consideration of resection margins. Guidelines recommend free margins of 3-5 mm, depending on the size of the lesions, to ensure adequate removal. Mohs micrographic surgery is particularly indicated for tumors located in critical areas or for lesions with higher infiltrative potential, especially where tissue preservation is essential. This procedure consists of removing the tumor layer by layer , followed by immediate microscopic analysis of the margins to detect any residual tumor cells. Excision is continued until histologic

negativity of the margins is obtained, thus ensuring complete excision of the tumor.This approach minimizes the risk of recurrence while preserving as much healthy tissue as possible—a considerable advantage for aesthetically significant areas [12-13].

Several studies indicate that radiotherapy could be an effective treatment option for skin cancer, especially for cases with inoperable lesions or as an adjuvant to surgery. This approach provides significant benefits both as a primary treatment for patients who are not surgical candidates and as a supplementary intervention to reduce the risk of postoperative recurrence and enhance disease control [12,14-15].

One of the key advantages of radiotherapy is its ability to preserve surrounding tissue integrity, avoiding scarring and anatomical defects, and thus minimizing the need for reconstructive surgery. Moreover, in highly sensitive and visible areas—such as the lips, nose, ears, and periorbital region—radiotherapy often yields better aesthetic outcomes than surgery.

The therapeutic effect of radiotherapy is based on the action of ionizing radiation, such as X-rays, which alters the DNA of cancer cells, inducing atomic and molecular instability. This disruption compromises cell survival, leading cancer cells to die predominantly during division, in a process known as mitotic death [16].

When ionizing radiation passes through a cell, it causes DNA damage through two mechanisms: direct and indirect action. Direct action occurs when radiation directly impacts the DNA molecules, immediately damaging their molecular structure and atomic bonds. In contrast, indirect action takes place when radiation ionizes water and oxygen molecules within the cell, producing highly reactive free radicals that subsequently chemically damage the DNA. As a result of the combination of direct and indirect damage, cancer cells do not die instantly; instead, they continue to divide a limited number of times before ultimately undergoing cell death. This delayed effect helps to explain both the potential late onset of radiotherapy side effects and why the treatment's effectiveness on the tumor may not be immediate.

Radiotherapy is particularly effective during the active phases of the cell cycle, especially during mitosis, as cells are more sensitive to DNA damage at these times. Cancer cells, which replicate rapidly and frequently, are therefore more vulnerable compared to normal cells that

divide less often. This selective action allows radiotherapy to primarily target cancer cells while minimizing the impact on healthy tissues [17].

For the treatment of the skin lesions analyzed in the study, superficial radiotherapy using low-energy X-rays (kV) was employed. This technique utilizes low-energy photons (ranging from 50 to 150 kV) to target superficial skin lesions. It is particularly indicated for small tumors (up to 3 cm in size), especially for lesions that do not exceed 5 mm in depth [17-18]. Furthermore, the use of low-penetration X-rays allows for the concentration of the maximum dose in the upper layers of the skin, thereby limiting exposure to the underlying healthy tissues. Depending on the characteristics of the lesion, different energy levels are selected (for instance, 50–75 kV for lesions up to 2 mm, and 100 kV for deeper lesions). The source to skin distance tpically ranges from 10 to 30 cm to accommodate the required depth.

The side effects of kV-based radiotherapy are classified as acute, such as skin irritation and desquamation, and late effects, which may emerge more than three months after treatment. The limited penetration of the photons into the tissues helps to preserve the underlying organs and bone structures, significantly reducing local toxicity while providing effective tumor control with favorable aesthetic outcomes [19].

1.3 OCTA in assessing skin response to radiotherapy

To monitor the progression of skin lesions during and after radiotherapy, this thesis focuses on a non-invasive monitoring approach based on Optical Coherence Tomography Angiography (OCTA) technology. This technique enables the volumetric representation of the vascular network within the target tissue without the use of contrast agents. Its non-invasive nature, combined with recent technological advancements, offering many advantages over other imaging methods [20].

The primary goal of this thesis is to acquire images of the skin lesion at three distinct time points: before radiotherapy, one month after treatment, and three months post treatment. By analyzing specific parameters such as vessel density and tortuosity within the vascular network, the aim is to identify any significant variations across the three stages and correlate these changes with the the therapeutic response and the effects of radiotherapy on the skin tissue.

OCTA technology combines structural and angiographic data, providing insights into both the morphology and composition of the skin tissue as well as the vascular network within it. It allows for the generation of co-registered images in both "en face" (top-down visualization directly observing the skin surface) and "cross-sectional" (sections revealing the different layers of the skin) formats, thus offering an integrated and detailed view of cutaneous microvascularization, facilitating the analysis of vascular changes associated with pathological conditions.

Unlike other techniques such as fluorescein angiography (FA) or indocyanine green angiography (ICGA), OCTA is completely non-invasive as it does not use exogenous contrast agents. This characteristic is particularly important as it reduces the risk of complications associated with invasive procedures and enables frequent monitoring of lesions safely for the patient [20]. Furthermore, the ability to perform repeated scans makes OCTA an ideal tool for the follow-up of skin lesions, allowing for continuous observation of vascular changes associated with treatment response without the need for repeated biopsies, which carry risks of scarring and do not permit ongoing visualization of the same area.

The vasculature gives important insights regarding the development and progression of skin tumors. The capability of tumors to create an independent vascular network supports tumor growth, providing essential oxygen and nutrients and increasing the possibility of metastasis. This process also facilitates tumor spread to other tissues. The morphology and tortuosity of the vasculature are not only indicators to distinguish healthy from cancerous tissues, but also provide information about tumor progression. In healthy tissues, blood vessel growth is a dynamic process that responds to the functional needs of the body. In tumors, however, the vasculature develops in response to the nutritional needs of the tumor itself through angiogenesis. This complex process includes migration and proliferation of endothelial cells, degradation of extracellular matrix, and formation of new blood vessels. Recent studies have shown that inhibition of angiogenesis can reduce tumor growth and limit metastatic spread [21-22].

To monitor vasculature changes in skin tumors, OCTA provides high-resolution imaging of epidermal and dermal microstructures up to a depth of about 1 mm, mapping of the vascular network. This is very important because alterations in vascularization may indicate angiogenesis processes associated with tumor growth, providing essential information on the

effectiveness of radiotherapy. Unlike OCT, which offers only structural images, OCTA provides visualization of blood flow and vascular morphology. Knowledge of vascular patterns in healthy skin is important for detecting changes associated with cancerous lesions. Malignant lesions, such as BCC, have a disorganized and tortuous vascular structure, with vessels crossing the epidermis and branching into thin capillaries [23-24]. The use of OCTA, therefore, is an advantage in the diagnosis and monitoring of cancerous lesions.

2. Materials and methods

In this section, the materials and methods used to conduct the thesis are described in detail, organized into various subsections, as illustrated in Fig 2.1. Initially, Optical coherence tomography (OCT) is presented (B), which represents the imaging technique used for acquiring the images. Subsequently, the study population (A) is described , consisting of five selected patients, with the indication of the relevant clinical characteristics for the study.

The following subsection is related to the image acquisition protocol (C), with a detailed description of the procedures for performing OCT scans.

Next, the image processing pipeline (D) is analyzed, covering all computational steps from the acquisition of raw data to the segmentation of the OCTA volumes. Finally, the vascular parameters extracted (E) from the segmented volumes are illustrated. The methods used to calculate and analyze the morphological and tortuosity parameters are described, highlighting the quantitative approach used to evaluate structure and complexity of the blood vessels.

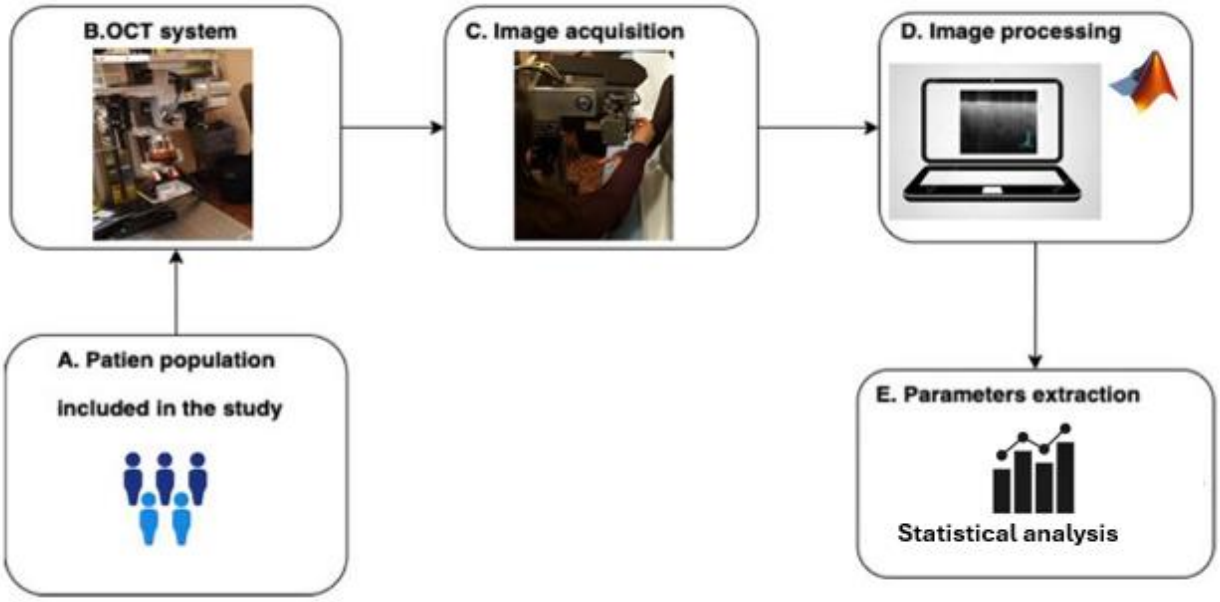

Figure 2.1 : Schematic summary of materials and methods workflow: (A) Patient population included in the study; (B) OCT system used for image acquisition; (C) Image acquisition protocol; (D) Image processing process; (E) Parameters extraction.

2.1 OCT system and OCTA reconstruction

All image acquisitions during the three sessions were performed using an Optical Coherence Tomography (OCT) system, utilized for research purposes at the Medical University of Vienna. Since OCTA is based on OCT technology, it is beneficial to provide a brief overview of the current OCT methodologies before exploring into the specific techniques of OCTA.

2.1.1 Principles of OCT

The functioning of OCT is based on the coherence of light, which is defined as the property that indicates how much two light waves are in phase and have a constant phase relationship over time. This characteristic allows for the detection of light reflected from tissue structures at depths that are not accessible using conventional microscopy techniques.

By employing a focused light beam, OCT compares the backscattered light from the sample with a reference beam coming from the same source. Only the photons that maintain their coherence, without being altered by interactions within the tissue, generate constructive interference, providing a meaningful signal for the detector. To capture the reflectance of the sample, an interferometer is used. This instrument divides the light into two separate paths: one directed toward the sample and the other toward a reference arm with a known length. The reflected light waves from both arms are then combined, and the observed interference indicates differences in optical path length [20].

In this way, OCT uses the temporal coherence of light to create reflectance profiles (A-scan) and cross-sectional images (B-scan). The technology offers several scanning modes that facilitate the reconstruction of a three-dimensional (3D) volume of the tissue. The A-scan provides one-dimensional analysis, while the B-scan combines multiple A-scans into a two-dimensional scan. The C-scan integrates various B-scans acquired at adjacent lateral positions, generating a 3D tomogram. By combining these modalities, OCT delivers a detailed representation of the internal structures of the analyzed tissue.

In this study, each B-scan comprises 512 A-scans, while a volume is made up of 512 B-scans. Once all B-scans are acquired, it becomes easy to visualize the cross-sectional images, which appear as two-dimensional representations in the yz plane. Additionally, en-face views can be obtained in the xy plane, allowing for a top-down perspective of the tomogram.

OCT techniques have evolved significantly, continuously improving acquisition speed, resolution, and depth penetration.

The first version, Time-domain OCT (TD-OCT), has significant limitations, such as slow acquisition and lower image quality due to noisy data. In TD-OCT, each single point of the image is acquired separately. This process involves physically moving the reference mirror to measure the time delay of the light signal reflected from the sample. In practice, the system's optics must continuously move to obtain the data for each point, which results in a very slow scan (Fig 2.2) [25-27].

This limitation led to the development of spectral-domain OCT (SD-OCT), which allows for the simultaneous acquisition of multiple points using a spectrometer that detects the spectrum of the reflected light. This approach improves speed, resolution, and tissue penetration. In SD-OCT, the interference signals are analyzed through Fourier transforms to generate high-resolution images without the need to physically move the reference mirror (Fig 2.2) [25-27].

Swept-Source OCT (SS-OCT), which is employed in my thesis project, represents a further advancement. SS-OCT is an advanced non-invasive imaging technique that uses a frequency swept laser and dual-balanced photodetectors to capture high-resolution images.

Swept-frequency lasers are important for high-resolution imaging in SS-OCT systems. These lasers modulate their frequency over a range of wavelengths, which allows precise depth measurements. By rapidly varying the frequency, they allow the system to acquire data quickly and with greater accuracy. However, the laser’s frequency sweep must be linear to avoid errors in distance measurement. Commercial swept lasers are generally affected by nonlinearity, which can distort the signal and reduce accuracy. To overcome this problem, methods such as k-clocking synchronize the sampling rate with the laser scan, improving accuracy and minimizing errors in the data. Significant progress has been made, with sweep rates now reaching up to tens of megahertz [28-29].

This technology allows for faster scanning and the use of longer wavelengths compared to SD-OCT, which enhances tissue penetration and overall image quality. These features help reduce motion artifacts and improve the signal-to-noise ratio (SNR), making SS-OCT particularly effective for detailed and reliable imaging (Fig 2.2) [25-26].

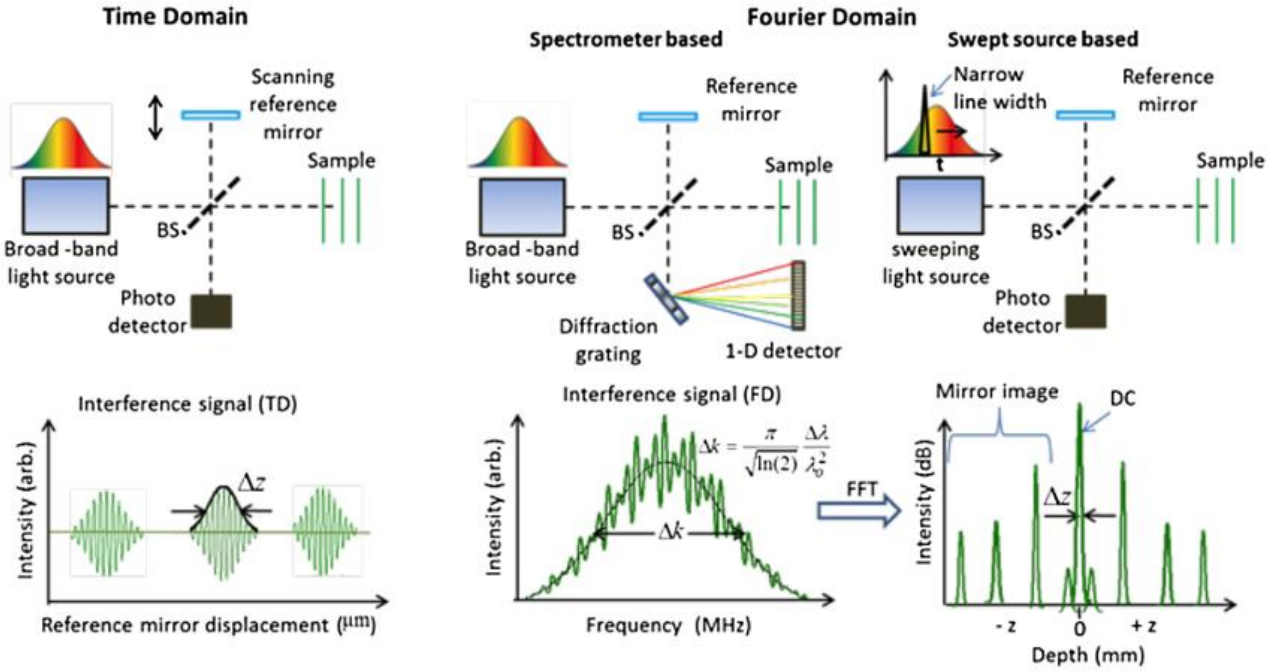

Figure 2.2: Schematic overview of the different OCT modalities. OCT systems are divided into time-domain (TD) and Fourier-domain (FD) systems. FD systems, can be classified into spectrometer-based and swept source systems. Source: [42]

2.1.2 Principles of OCTA

OCTA represents a significant advancement in vascular imaging, extending the capabilities of OCT to visualize blood flow and vascularization. This technique is notable for its ability to reveal contrast generated by the movement of blood cells, particularly erythrocytes, which serve as dynamic components within the circulatory system. Unlike static skin structures such as the epidermis and dermis, blood within blood vessels is in motion, allowing for the detection of significant variations between acquired images.

The functioning of OCTA is based on the repeated recording of B-scans from the same position. During this process, the scans are compared pixel by pixel, enabling the identification of signal differences caused by blood flow. Subsequent images are analyzed

to calculate decorrelations and dissimilarities, which measure the differences in movement between the acquired images. These measurements provide information on variations in blood flow and facilitate the generation of cross-sectional representations of microvascularization [20].

Motion contrast algorithms: There are several algorithms that can be used to generate motion contrast signals for OCTA, which are based on signal amplitude, phase, or both. This study employs the intensity-based method, which utilizes the amplitude of Fourier-transformed data to calculate motion contrast. This approach involves analyzing the differences between sequentially acquired intensity images, allowing for the generation of a contrast volume that reflects variations in blood flow. A significant advantage of this method is its low sensitivity to phase noise and artifacts, making it preferable for many clinical applications.

Acquisition times: Each B-scan is acquired in sequence, with the total acquisition time determined by the acquisition rate of the A-scans multiplied by the number of A-scans per B-scan. After each B-scan, the OCT beam must be quickly repositioned to its initial position without acquiring any data. B-scans are repeated after a delay ΔT, which represents the inter-scan time. This time is important for OCTA to detect blood flow.

Longer inter-scan times increase sensitivity to slower blood flows but can lead to signal saturation in faster flows. This means that when the flow is rapid, the system has difficulty distinguish signal variations because blood cells move quickly and may travel out of the light beam between scans, making it difficult to detect the same cells in consecutive scans. Conversely, shorter inter-scan times better capture fast flows but may reduce sensitivity to slower flows [20].

In this thesis, a scanning frequency of 222.2 kHz is used. Each B-scan has 512 A-scans and 512 B-scans are collected consecutively to form a volume.For each position, four consecutive B-scans are acquired, leading to the creation of four volumes for each OCTA reconstruction.

The frame rate is calculated by dividing the scanning frequency by the product of the number of A-scans per B-scan (512), the number of B-scans per volume (512), and the number of volumes (4).

Advantages and Limitations: One of the main advantages of OCTA is its non-invasiveness, an important characteristic in clinical settings and fundamental for this study, as this technology allows for the monitoring of radiotherapy treatment without the need for contrast agents (Fig 2.3). Traditionally, visualizing blood flow required the injection of contrast agents, while OCTA offers a revolutionary solution by enabling the observation of blood vessels with high resolution down to the capillary level, eliminating the need for injections[20]. Additionally, since OCTA utilizes non-ionizing radiation, it is completely safe when properly employed and poses no exposure risks to the patient.

In contrast to fluorescence angiography (FA) or indocyanine green angiography (ICGA), OCTA does not experience issues of hyperfluorescence caused by contrast leakage, thus providing high-contrast, well-defined images of microvascularization. The volumetric data acquired can be segmented to visualize individual vascular layers separately, allowing for a detailed representation of capillary networks and the extraction of parameters indicative of vascular density and complexity.

However, OCTA also has some limitations. Because it relies on motion contrast to visualize microvascularization, it requires multiple scans at the same location to obtain reliable images, which consequently increases acquisition times compared to structural OCT. Furthermore, the quality of OCTA images can vary significantly depending on the equipment, scanning protocols, and processing algorithms used. OCTA images are particularly affected by artifacts, such us motion artifacts and projection artifacts. This artifacts require specific correction procedures for accurate interpretation.

Figure 2.3: Image of the OCT system used for skin image acquisition. The image shows the positioning of the OCT device on the skin surface and the path of the light beam during the acquisition process.

2.2 Demographic and clinical data

Patients were recruited at the Medical University of Vienna, where the necessary ethical approval for conducting the study was obtained. Five patients were recruited, with a total of 12 lesion volumes analyzed. Each patient was treated with radiotherapy, and the lesions were examined by OCT at three separate time points: before treatment, one month after treatment, and three months after treatment.A total of 9 lesions were analyzed across these volumes. One lesion from the fifth patient was divided into three volumes to cover the entire area, bringing the total number of lesion volumes to 12. Additionally, for each patient, a portion of healthy skin was examined in each acquisition, resulting in a total of 10 volumes dedicated to healthy skin. All skin cancer diagnoses were confirmed through biopsy, which involved the collection of tissue samples from the lesions for histopathological examination.

- The first patient (ST001), a female, presented four lesions in Fig 2.4 : three actinic keratoses (AK) on the left leg, characterized by rough, scaly patches typical of sun-damaged skin and one lesion on the right leg identified as SCC, noted for its ulcerated appearance and potential for local invasion.

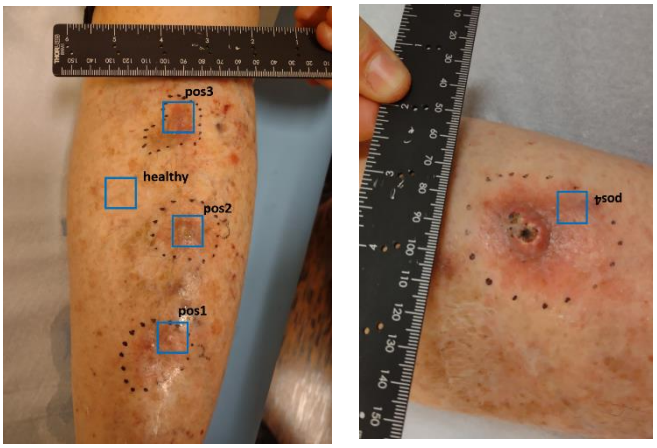

Figure 2.4: Image of lesions in positions 1, 2, 3, and 4 of patient ST001.

- The second patient (ST002), a male, had a BCC lesion in the acromial region presented in Fig 2.5. During the acquisition sessions, difficulties emerged in the correct positioning of the OCT device due to the location of the lesion, which did not allow optimal contact between the area to be acquired and the device glass. This led to artifacts in the images, making the data from the first acquisition unreliable. As a result, the data collected before radiotherapy were excluded from the analysis. However, the data from the healthy skin and form the second and third acquisitions, after the treatment, were included in the analysis.

.

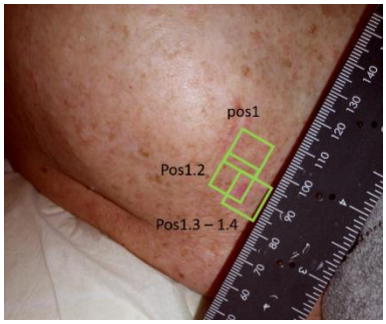

Figure 2.5: Image of lesion of patient ST002.

- The third patient (ST003), also male, presented two BCC lesions in Fig 2.6: one located on the right side of the forehead and the other on the left side of the forehead.

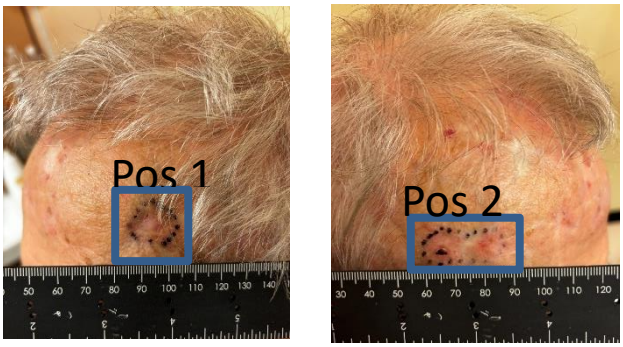

Figure 2.6: Image of lesions in position 1 and 2 of patient ST003.

- The fourth patient (ST004) had an SCC lesion on the left ear, which was examined in two distinct volumes, one focusing on the front and the other on the back of the lesion (Fig 2.7). Again, the position of the lesion did not allow for optimal contact between the skin and the device, leading to artifacts in the acquired images. Therefore, the data from the third acquisition were excluded from the analysis dataset, as a reliable analysis could not be performed.

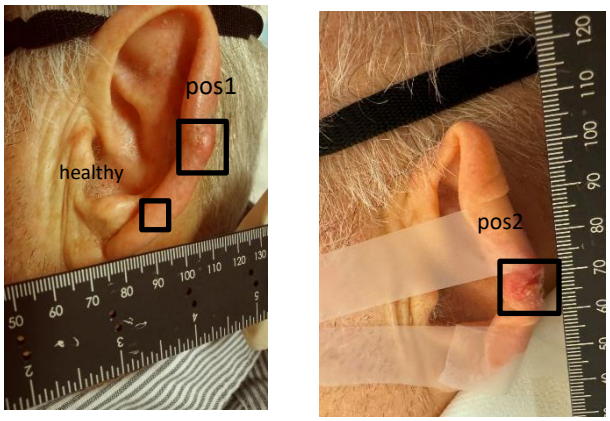

Figure 2.7: Image of lesion of patient ST004.

- The fifth patient (ST005) presented a BCC lesion on the left leg in Fig 2.8, which was analyzed in three distinct volumes, covering the entire area of the lesion to ensure a comprehensive evaluation.

Figure 2.8: Image of lesion of patient ST005.

The data are summarized in Table 1, where, for each patient, the number of volumes analyzed for lesions and for healthy skin is specified. In particular, for each time point, the number of acquisitions made for lesions and corresponding areas of healthy skin are shown.

It is important to specify that a single lesion may be divided into multiple sub-volumes to enable a comprehensive analysis.This approach,for example, was applied to patient ST005. In some cases, as with patient ST002, ST003, ST004, where a lesion has been acquired in multiple positions, the sub-volume with the highest quality and fewest artifacts was selected to ensure maximum reliability in the results.

Patient	Number of acquisitions		
	First session	Second session	Third session
ST001	4 lesions + 1 healthy	4 lesions + 1 healthy	4 lesions + 1 healthy
ST002	1 lesion	1 lesion	4 lesions + 1 healthy
ST003	2 lesions	3 lesions + 1 healthy	5 lesions + 1 healthy
ST004	3 lesions + 1 healthy	3 lesions + 1 healthy	3 lesions + 1 healthy
ST005	3 lesion + 1 healthy	3 lesions + 1 healthy	3 lesions + 1 healthy

Table 1: Number of acquisitions performed for each session. Additionally, an OCTA image of healthy skin was acquired for each patient.

2.3 Image acqusition

In this section, the acquisition protocol applied during the imaging sessions of patients using optical coherence angiography (OCTA) is described. The imaging protocol consists of a set of instructions and procedures that guide the image acquisition process, ensuring accurate and reproducible results.

- **Safety:** During the imaging sessions using OCT, safety measures were implemented to protect both patients and operators, particularly due to the presence of a laser classified as Class 3B. Therefore, it is recommended that all patients wear protective glasses that are designed to shield the laser for the entire duration of the acquisition. This precaution is important to avoid eye damage from accidental exposure to the laser beam. In addition, operators are required to wear disposable gloves during procedures to ensure hygiene, and the use of protective gowns is recommended. The lens of the device is sterilized before and after each acquisition. This process is important to maintain a sterile environment during procedures.

- **Calibration:** Calibration of the laser is a fundamental step to ensure the accuracy and reliability of the imaging system. It is important to optimize the laser parameters to compensate for any losses in the optical system and correct distortions. Each time the laser is activated, a calibration is performed to determine which pixels of the image are valid and should be considered during data acquisition, and which pixels contain noise or are unreliable and should therefore be excluded. At the end of the calibration process, a text file (*DVV file*) is generated containing information about the valid pixels of the OCT image. This file is essential as it guides the data analysis, ensuring that only valid pixels are taken into account for an accurate evaluation of the acquired images. It is important to note that calibration must be performed for each acquisition session to guarantee consistent and reliable results.

- **Experimental Setup:** The patient is positioned on a patient bed. Before acquisition, a photograph of the lesion is taken with ruler to provide information about the morphology and dimensions of the lesion. The acquisition device has a 1 mm thick glass that is placed between the probe and the skin surface, helping to reduce the phenomenon of skin hyper-reflection. It is very important to be sure that the entire skin surface is in contact with the glass to optimize the quality of the acquisition. A small amount of distilled water is also applied between the glass and the skin to improve the refractive index match between the two materials. It is better if the water is uniformly distributed, beacuse this helps to ensure higher quality data acquisition.

- **Acquisition:** Once the acquisition system is ready (Fig 2.9) and the probe (Fig 2.10) is in contact with the skin, an image of a B-scan can be displayed on the screen. From the preview observed, adjustments can be made to several parameters to enhance the quality of the visualization. The display scale is adjusted within the system, while focus is fine-tuned using the device itself. To avoid reflection phenomena from the skin surface, the laser beam is tilted relative to the vertical axis through the device settings. At this point, the acquisition process begins. It is better to acquire the same lesion many times at nearby positions to have alternatives available in case one of the acquisitions contains numerous artifacts.

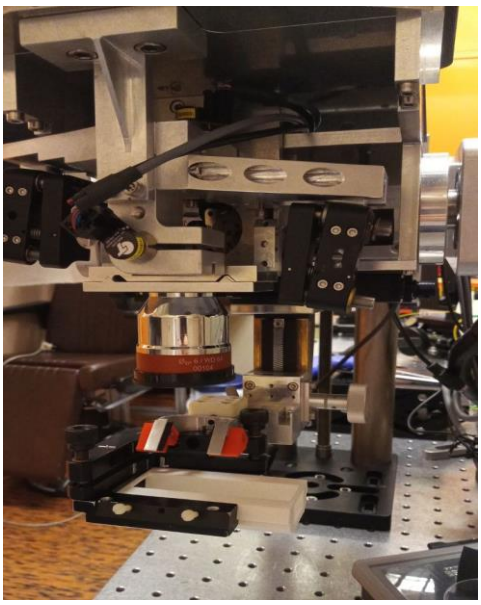

Figure 2.9: Image of the OCTA device within the laboratory setting.

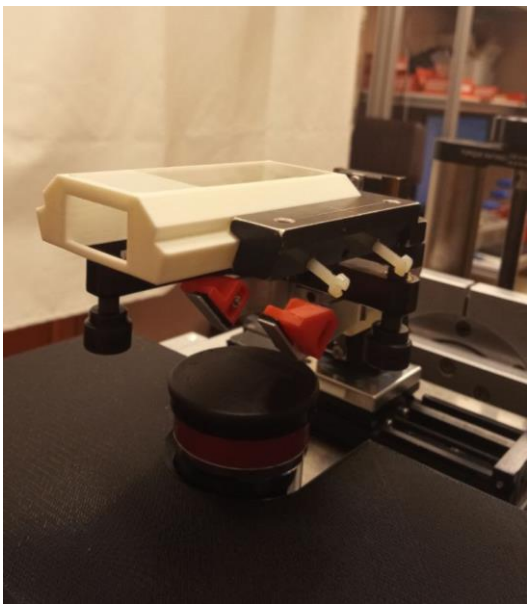

Figure 2.10: Image of the OCT device probe.

2.4 Image processing and segmentation

The image processing pipeline is explained in Fig 2.11, illustrating the path from the raw data acquired to the segmented volume.

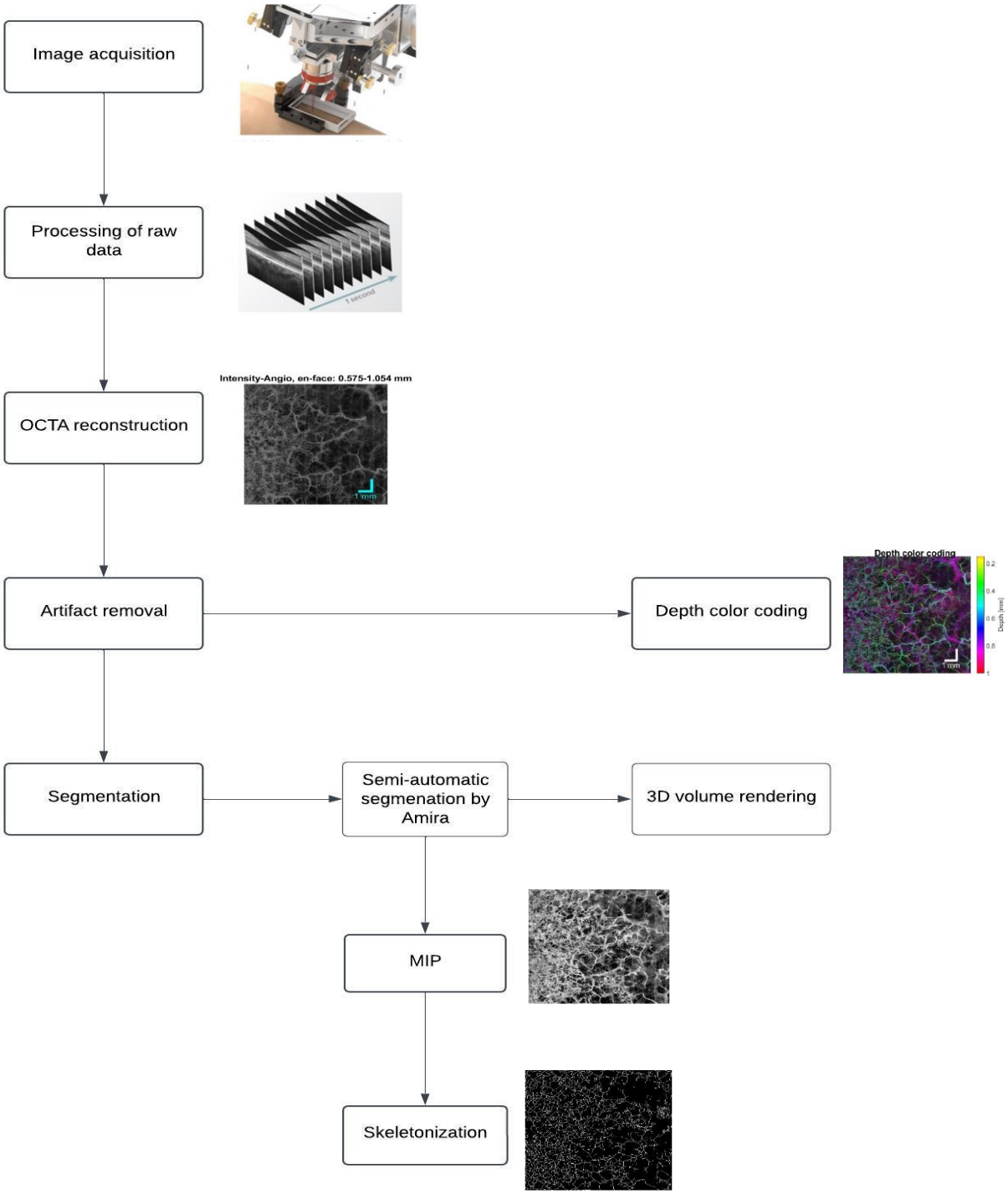

Figure 2.11: Flow chart showing the image processing pipeline.

2.4.1 Processing of raw data

The first phase of the image processing pipeline involves preprocessing the acquired data, which are organized into OCT data matrices. During this phase, several parameters are defined that determine the resolution and structure of the data to be processed. These parameters include the size of each voxel in millimeters, which establishes the spatial resolution of the image, and the dimensions of the matrices, expressed in terms of A-scans and B-scans, indicating the number of points (A-scans) and the number of cross-sectional scans (B-scans) respectively. Additionally, a region of interst (ROI) is selected to limit the analysis to the relevant sections of the acquired data, reducing computational complexity and processing time.

The data collected by the OCT system are organized into 32 files, each containing data from 64 B-scans. Since the number of B-scans acquired at the same position is 4, each file consists of 16 groups of B-scans from different positions. For the code to function correctly, a DVV file is also required.

To reduce background noise and improve image homogeneity, a background subtraction process is applied. This is achieved by calculating the average pixel values at a specific depth (the i-th row or level) of the B-scan and subtracting this average value from each pixel in the same row. This technique of horizontal mean subtraction significantly reduces irrelevant intensity variations, eliminating background noise without requiring separate acquisitions for the background, which would increase the data load to manage and process.

Next, zero padding is applied to the data matrix by adding rows of zeros above and below it. This step increases the frequency resolution during the following Fast Fourier Transform (FFT), facilitating the interpretation of spectral components. Further improvement is achieved by windowing, which reduces the effects of discontinuity at the signal boundaries that can cause spectral artifacts. The window, applied as a multiplier to the signal, gradually attenuates the values at the boundaries and minimizes distortion.

After windowing, FFT is done to move from the time domain to the frequency domain, thus obtaining the intensity components of the signal. After this, the redundant half of the signal is removed, keeping only the useful part of the frequencies. At this point of processing, a

dataset made up of complex numbers is obtained, which is the result of the FFT applied to the raw data to convert it into the frequency domain.

2.4.2 OCTA reconstruction

The next step involves reconstructing the OCTA volume using the intensity-based method. The main steps include:

- The volume is divided into four sub-volumes, each representing OCT scans acquired at different times.
- The B-scan scans and cross-sections of the first sub-volume are displayed using graphical representations to facilitate analysis (Fig 2.12).
- The angiographies are reconstructed by calculating the intensity differences between sequential sub-volumes, highlighting movement and areas where changes have occurred.
- A median filter is used to help detect the skin surface in the images and compensate for any tilt of the glass slide. The surface is found by analyzing the A-lines; the first pixel that exceeds a defined intensity threshold is identified, marking the beginning of the glass slide. A polynomial fitting curve is applied to these points and the obtained curves are used to establish a reference plane. Once the surface is identified, it is used to realign the volumes to a horizontal level.
- Visualization of the en-face image of the angiography and the en-face image of the OCT at different depth ranges (Fig 2.12).

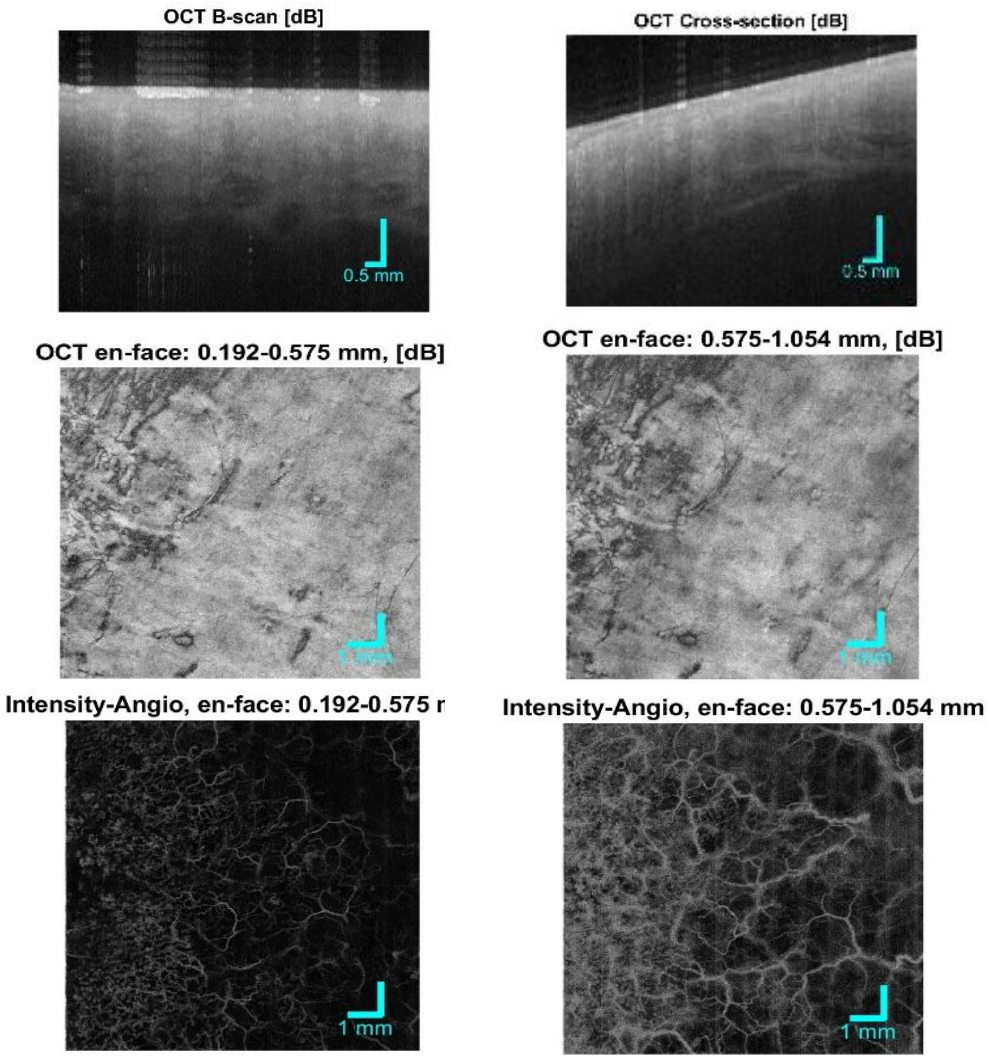

Figure 2.12: OCT B-scan , OCT cross-section, OCT en face at different depht ranges, OCTA en face at different depth ranges.

In OCT images, the structure of the skin may change depending on the region of the body, but the epidermis and the dermal-epidermal junction (DEJ) are generally recognizable. In cross-sectional images of healthy skin, the most superficial layer, i.e., the stratum corneum, appears as a highly reflective narrow band generated by the reflectivity of the skin surface. Importantly, this stratum corneum is easily distinguishable in images obtained from palmoplantar skin, where it is significantly thicker compared to other skin areas.In other regions of the body, where the stratum corneum cannot be identified, the epidermis can be observed as a granular band of variable thickness. The DEJ can be identified due to a marked variation in intensity between the epidermis and the papillary dermis; below the DEJ, there

is a transition to a lighter area corresponding to the dermis (Fig 2.13). Blood vessels are typically distinguished in the image as signal-free, round or elongated in shape [30- 31].

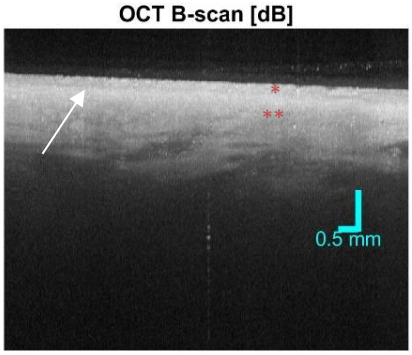

Figure 2.13: OCT B-scan. The arrow indicates the dermal-epidermal junction (DEJ), while * marks the epidermis and ** denotes the dermis.

En face images typically reveal a well-defined and organized vascular pattern in healthy skin. However, the appearance of blood vessels in OCTA images may vary between different areas of the body and may be affected by the presence of skin disease or injury. In particular, tumor cells tend to organize abnormally compared with healthy cells, contributing to this variability in vessel appearance (Fig 2.14) [31-32].

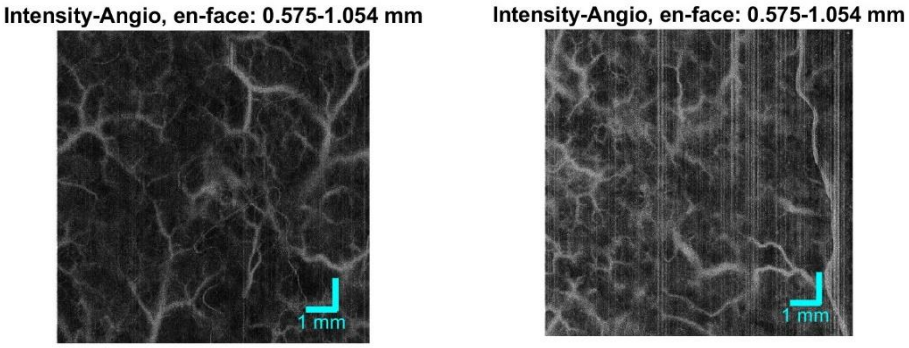

Figure 2.14: OCTA en-face of healthy skin (left) and OCTA en face of the lesion (right).

2.4.3 Artifact removal

The removal of artifacts is an important step in the reconstruction of OCTA volumes, as these artifacts can compromise the quality and accuracy of the obtained images. Below are the main types of artifacts and the associated removal techniques used:

- **Motion Artifacts:** A white line correction is performed to normalize signal intensities along the depth. This correction involves normalizing each B-scan against the average of all acquired B-scans. This approach helps to homogenize intensities, reducing variations caused by fluctuations in laser power and improving the overall quality of the images (Fig 2.15).

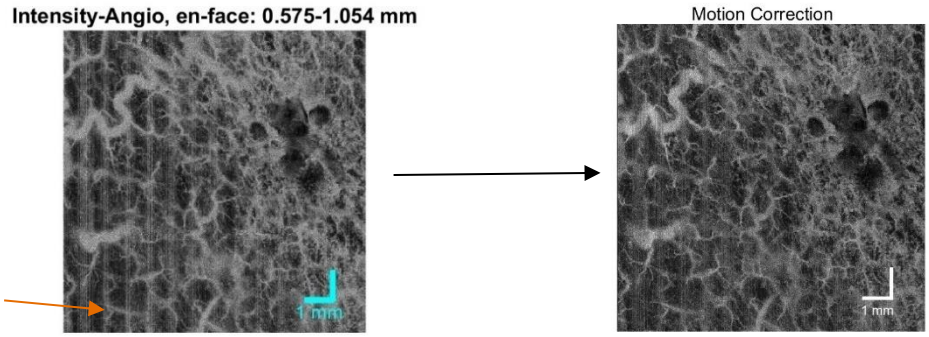

Figure 2.15: On the left, OCTA image showing motion artifacts, with the white lines indicated by the orange arrow. On the right, the same image after the removal of the artifact.

- **Projection Artifacts:** These artifacts primarily occur in the presence of highly reflective surface structures in the sample, such as superficial blood vessels, which can project artifacts into deeper images, obstructing the visualization of underlying structures. As light penetrates the tissues, the characteristics of the overlying structures affect the light reaching the deeper structures. In the case of blood vessels, the transmitted light exhibits variable fluctuations over time. Even if the characteristics of the underlying tissue remain constant, changing illumination can induce decorrelation between images from different B-scans, leading to a misleading impression of blood flow in reflecting layers beneath a vessel. To remove projection artifacts, a step-down exponential method is used. This method attenuates the intensity of superficial vessels in deeper images by applying an exponential decay function defined by the attenuation parameter γ, reducing projection artifacts [33] (Fig 2.16).

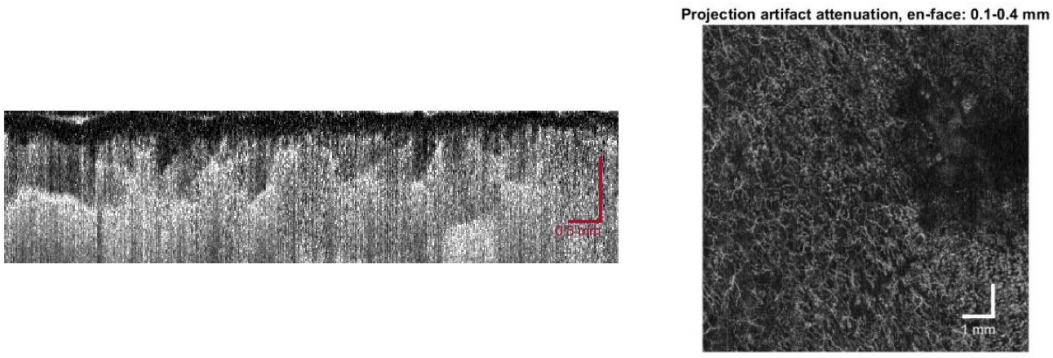

Figure 2.16: Left: Projection artifact on a B-scan view. Right: Projection artifact on an en-face view.

- **Filtering:** A median filter is applied to eliminate noise from the OCTA images. This filter works by replacing each voxel in the data with the median value of its surrounding voxels within a defined neighborhood. In this case, a 3x3x3 cube is used, capturing a local neighborhood around each voxel and calculating the median intensity. This approach effectively reduces high-frequency noise, such as "salt-and-pepper" noise, without significantly blurring the image.

- **Contrast Adjustment:** Finally, contrast adjustment is carried out using a luminance method, optimizing the visualization of the images by highlighting vascular structures and enhancing their interpretability

All steps of the artifact removal pipeline are presented in Fig 2.17.

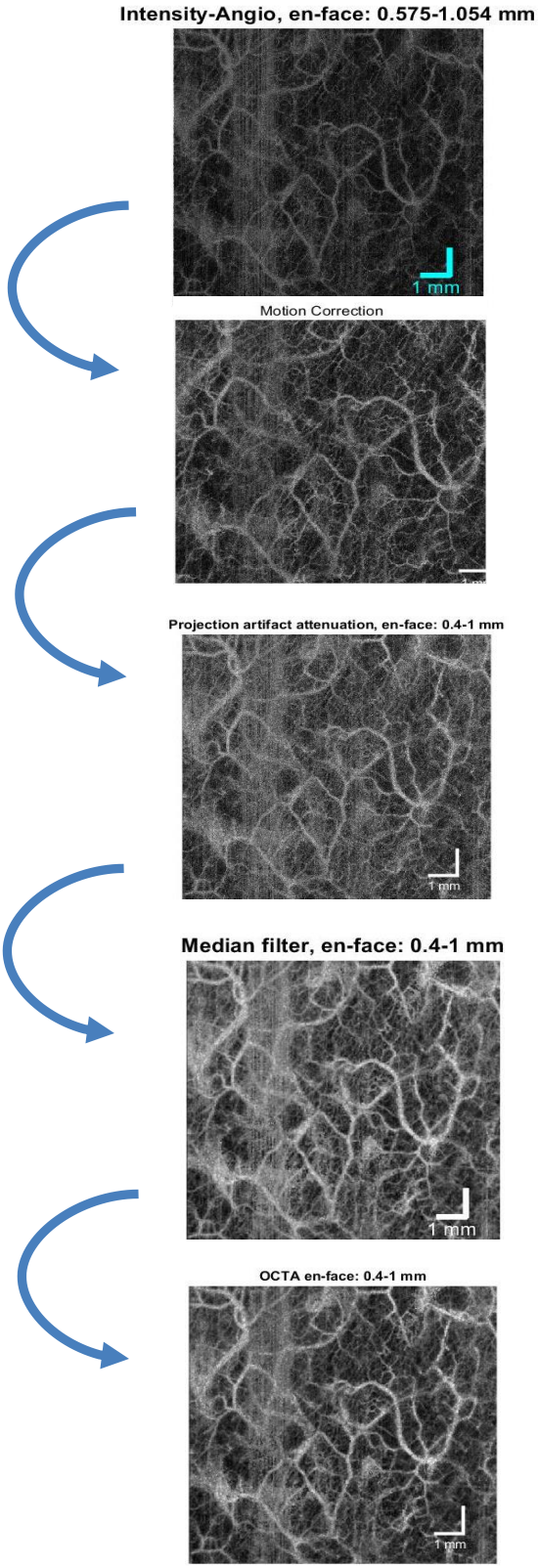

Figure 2.17: En-face images at different steps of the artifact removal pipeline.

2.4.4 Depth color coding

Depth color coding is a fundamental technique used in image visualization, as it allows for the representation of depth information in an easily interpretable format, as shown in Fig.2.18. To implement this technique, a color map is utilized, specifically the HSV map (Hue, Saturation, Value). Each depth level in the OCTA scan is assigned a distinctive color, facilitating the visualization of vascular structures at different depths. Additionally, the depth value is clearly represented on the color bar axis, providing an immediate visual reference.

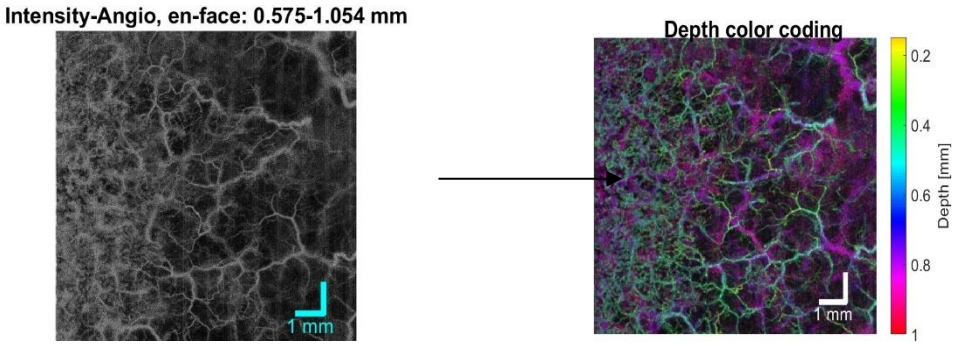

Figure 2.18: Representation of intensity angiographic images together with corresponding depth color coding maps.

2.4.5 Segmentation

After removing artifacts from OCTA images, the next step is semi-automated segmentation, which is performed using Amira software. This software allows to view the volumetric rendering of the reconstructed OCTA volume, both before and after segmentation, and to examine single slices using the "clipping plane" command.

Segmentation is very important for vasculature analysis, as it allows blood vessels to be isolated and highlighted. This step is done by choosing a threshold that identifies pixels that exceed it, thus facilitating visualization of the vessels.

It is important to choose an appropriate threshold for segmentation, especially in the case of noisy images. In some cases, it is better to exclude a few vessels rather than include excessive noise, in order to have a clearer visualization. For more accurate segmentation, Amira allows to observe the effect of the threshold on each slice of the volume, removing slices with too many artifacts. A common artifact in the first lateral B-scan of the xy plane is removed during this step. Next, the “remove islands” option allows isolated pixels to be removed; the size of the pixels to be removed can be chosen manually, and through the

“compute highlight” option a preview of the 2D segmentation without these pixels is displayed to decide if the pixel size should be changed. The result is a cleaner volumetric rendering. The "lasso" tool can be used to manually remove artifacts or bubbles present in the 3D representation.

After removing artifacts, the segmentation result is examined across all slices, from the superficial to the deeper one. If necessary, a smoothing process can be applied using the “smooth labels” tool to merge smaller objects.However it is important to do this carefully so as not to remove small vessels. Usually, this tool is applied only in the noisiest slices.

Finally, the volumetric rendering of the segmented volume can be viewed to check whether the result obtained is satisfactory or whether further modifications are needed. An example of volumetric rendering after segmentation is presented in Fig 2.19.

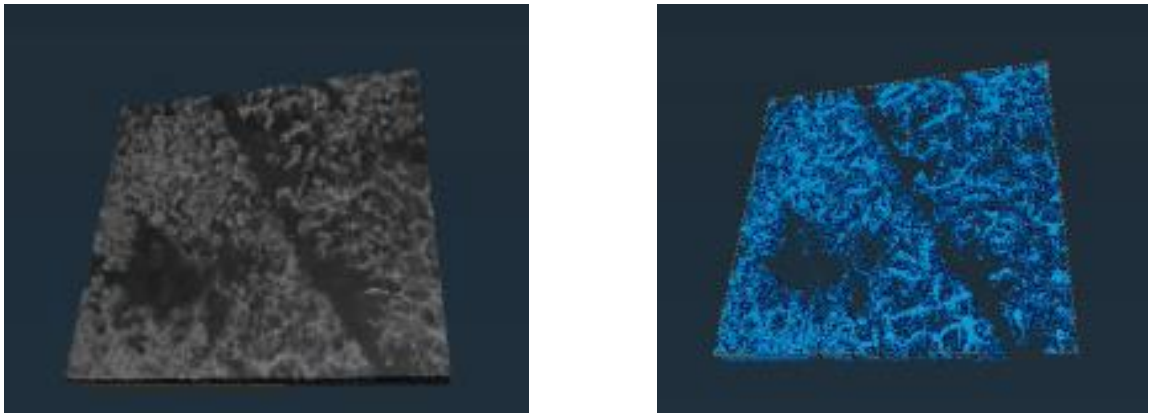

Figure 2.19: Volumetric rendering representation on Amira.

After obtaining the segmented volume, the next step is skeletonization, which is the extraction of the vessel skeleton. Although the skeleton can be generated directly from the 3D segmented volume, in my thesis work we preferred to extract it from 2D images for greater accuracy. The transition from the 3D segmented volume to a 2D image was achieved using the MIP (Mean Intensity Projection) technique. This is calculated by taking the average of voxels along the x-axis, generating an en face image in which each pixel represents the mean intensity along that axis. Normalization of the image allows values between 0 and 1 to be represented for better visualization. Before extracting the skeleton, a threshold is applied to the MIP. In most cases, Otsu's threshold, a non-parametric and unsupervised image segmentation technique that determines an optimal threshold by maximizing the separability between pixel classes in grayscale levels using cumulative

moments of the image histogram, has proven satisfactory [34] . However, in situations with a higher presence of artifacts, a threshold of approximately 0.35 was adopted [35]. This threshold was chosen to help reduce artifacts, accepting some loss of vascular data as a trade-off. Finally, the skeleton of the MIP is obtained based on the threshold applied (Fig 2.20).

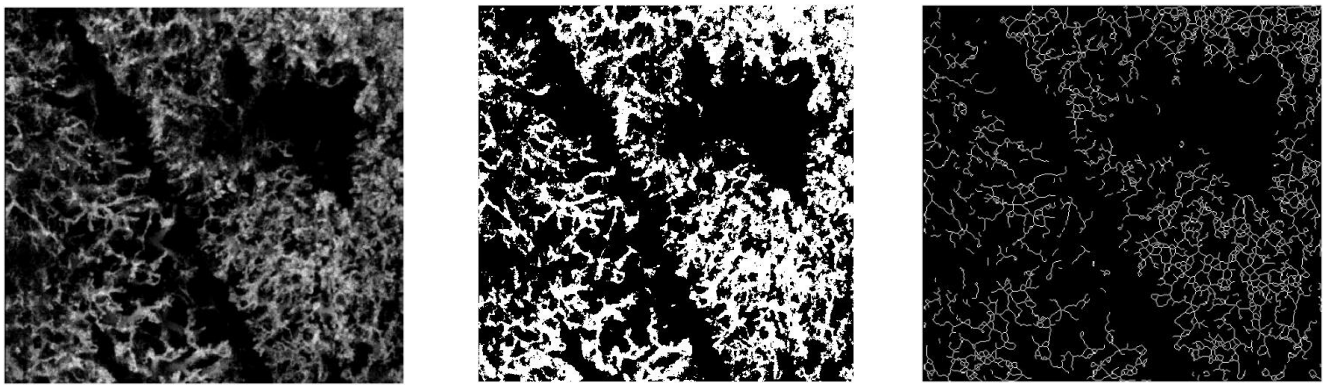

Figure 2.20 : From left to right, the image shows the MIP (Mean Intensity Projection), the MIP after thresholding, and the extracted skeleton.

2.5 Vascular parameters extraction

The process of extracting vascular parameters is essential for monitoring lesions in the context of this study. The aim of the thesis is to analyze changes in the lesions at three distinct time points: before treatment, after treatment, and three months after radiation therapy. However, simple visualization of the images does not provide all the necessary information for an accurate assessment. Extracting specific vascular parameters allows for a quantitative analysis of the blood vessel images and a numerical characterization of the vascular network, providing useful data for a deeper understanding of the vascular structure associated with the lesions. Several parameters are extracted for the morphological evaluation and tortuosity of the blood vessels. In particular, the following parameters have been analyzed:

- Vessel density
- Vessel radius
- Sum of angles metric
- Distance metric
- Inflection count metric
- Number of trees
- Number of branches

Vessel density (VD) is a morphological parameter that indicates the proportion of blood vessels within a specified area, calculated as the ratio between the pixels representing the vascular network and the total number of pixels within the region of interest (ROI). In this study, VD is measured using both 2D segmentation (VD mip) and the skeleton extracted (VD skel).

This parameter reflects the level of vascularization in a given area, independent of the distribution or individual structure of vessels. VD is a key indicator in OCTA imaging for assessing and comparing vascularization across different tissue regions, allowing for a reliable distinction between healthy and pathological areas. Additionally, vessel density enables monitoring of lesion progression at multiple time points, as it is closely correlated with the state of lesion progression or regression [35-37].

The **vessels radius** is an important morphological parameter for analyzing blood flow changes. Alterations in vessel diameter and wall thickness serve as indicators of changes in

flow dynamics and vascular functionality, which are especially pronounced in the presence of tumors or other pathologies.

To calculate vessel radius, MATLAB's *bwperim* function is applied to the binary vessel model to extract the perimeter of the vascular structure. This process identifies the vessel contours, serving as the basis for radius calculation. Then, the *bwdistgeodesic* function is used to compute the geodesic distance from each point on the perimeter to the vessel skeleton, taking into account the vessel's geometry. The resulting distance values are organized in a matrix, from which the radius values are extracted, including only those that are positive and finite.

The **Number of Trees** (NT) and **Number of Branches** (NB) are key morphological parameters used to characterize the structure of vascularization in tissues, providing insights into the complexity and organization of the vascular network. Blood vessel networks follow a branching topology comprising vascular "trees" and connecting vessels that form a complex, interconnected system. Collateral vessels, or arcades, connect branches of these trees, creating alternative pathways for blood flow. This organization allows the vascular system to adapt to changes in blood flow, thereby optimizing the delivery of oxygen and nutrients in both physiological and pathological conditions. As a result, this dynamic system can effectively respond to such changes [38-39].

Each vascular tree represents an independent blood distribution pathway, while branch points are essential for blood flow distribution, ensuring that it reaches different areas of the tissue. Within this thesis, the Number of Trees (NT) quantifies the number of independent vascular trees within a region of interest (ROI), while the Number of Branches (NB) measures the number of branches within the same structure. Assessing both parameters provides an estimation of the vascular network's complexity and efficiency.

In this study, specific MATLAB functions such as *bwmorph3* are used to identify branch and endpoint nodes within the vascular network. These points, crucial for analyzing structural organization, represent the primary coordinates of the network. The *bwconncomp* function is applied to identify the connected components of the vascular system, excluding very small objects (less than 20 pixels) considered to be noise. This vascular network analysis, based on these algorithms, allows a precise evaluation of vascular complexity and efficiency within the ROI.

The tortuosity of blood vessels is another important parameter that describes their shape, especially for identifying structural changes that may indicate malformations or disease. Malignant tumors, for example, can induce abnormally tortuous vessels, making tortuosity quantification critical for therapeutic monitoring of such diseases. Tortuosity is a geometric feature that can be quantified using several parameters that assess vessel curvature and complexity. Among the most commonly used metrics for measuring tortuosity are the **Distance Metric** (DM), the **Inflection Count Metric** (ICM), and the **Sum of Angles Metric** (SOAM). These parameters offer complementary insights into the geometric characteristics of blood vessels, aiding in a deeper understanding of their structural complexity [40-41].

The **Distance Metric** (DM) is the most commonly used metric for quantifying blood vessel tortuosity. It is calculated as the ratio between the actual path length of a vessel (L) and the Euclidean distance (D) between its two endpoints. This metric provides an indication of how much the vessel path deviates from a straight line: a value of 1 indicates a straight vessel, while values greater than 1 suggest increasing tortuosity. However, DM does not account for the frequency and intensity of directional changes along the vessel path, making it more sensitive to general curvature rather than sharp directional shifts.

To address this limitation, the **Inflection Count Metric** (ICM) was introduced. This metric multiplies the DM by the number of "inflection points" along the vessel curve, which are points where the curve changes concavity, switching from convex to concave or vice versa. The presence of multiple inflection points increases the ICM value, making it more sensitive to frequently oscillating curves and more representative of vessels with noticeable directional changes.

Lastly, the **Sum of Angles Metric** (SOAM) calculates the sum of angles formed by the tangent at each segment along the vessel path. This metric measures the degree of directional change at each point and is particularly useful for characterizing vessels that follow a spiral path or present complex curvatures. Unlike DM, which focuses on the path length relative to the straight-line distance, and ICM, which considers inflection frequency, SOAM captures the vessel's directional behavior across its entire course.

In summary, while DM provides a measure of path distance compared to linear length, ICM accounts for the frequency of concavity changes along the vessel, and SOAM captures directional changes along the vessel's path, as shown in Fig 3.1.Combined analysis of these

parameters provides a comprehensive assessment of vascular tortuosity, helping to better understand alterations in the vascular network and to distinguish between physiological and pathological conditions.

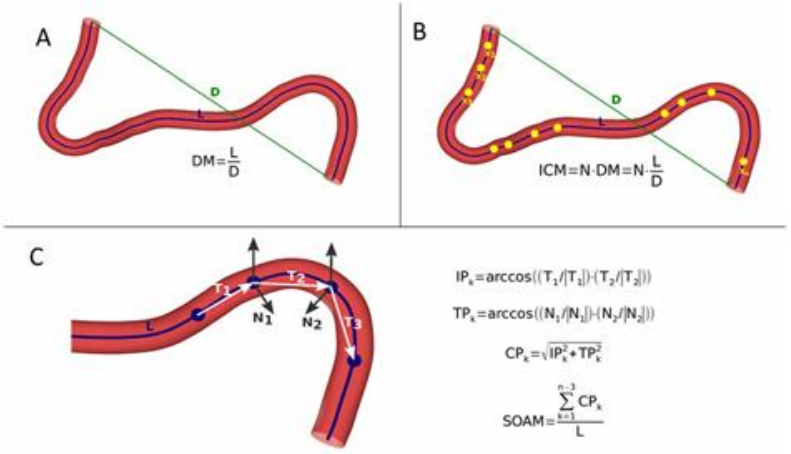

Figure 3.1: Illustration of the method used to calculate the three tortuosity parameters: (A) distance metric, (B) inflection count metric, and (C) sum of angle metric. Source [41]

The parameters are not calculated over the entire two-dimensional image; instead, the image is divided into regions of interest (ROIs), resulting in a total of 16 ROIs . This division allows for the calculation of parameters ROI by ROI, preserving the structure of the image and facilitating the comparison of parameters across the three acquisition sessions.

To visualize the extracted parameters, heatmaps have been created, in which the values of the parameters in different locations of the image are represented using colors. For the creation of the heatmaps, the matrices containing the parameter values for each pixel were normalized to a range from 0 to 1. Initially, a min-max scaling method was applied, where the parameter values were scaled based on the minimum and maximum values present in each matrix. Subsequently, a patient-based normalization was adopted, where min-max scaling was performed considering the maximum and minimum values for each parameter, taken as the highest and lowest values observed across all lesions and during all acquisitions for each patient. This approach helps maintain consistency in the normalized values and facilitates comparison between the different acquisition sessions.

Initially, the parameters and heatmaps were generated without overlapping the ROIs (Fig 3.2); successively, a 30% overlap was adopted. In the overlapping areas, the parameter

values were calculated as the average of the two adjacent ROIs.This was done to achieve a smoother representation in the heatmaps, avoiding sharp color changes that might result from sudden changes in the parameter values (Fig 3.3).

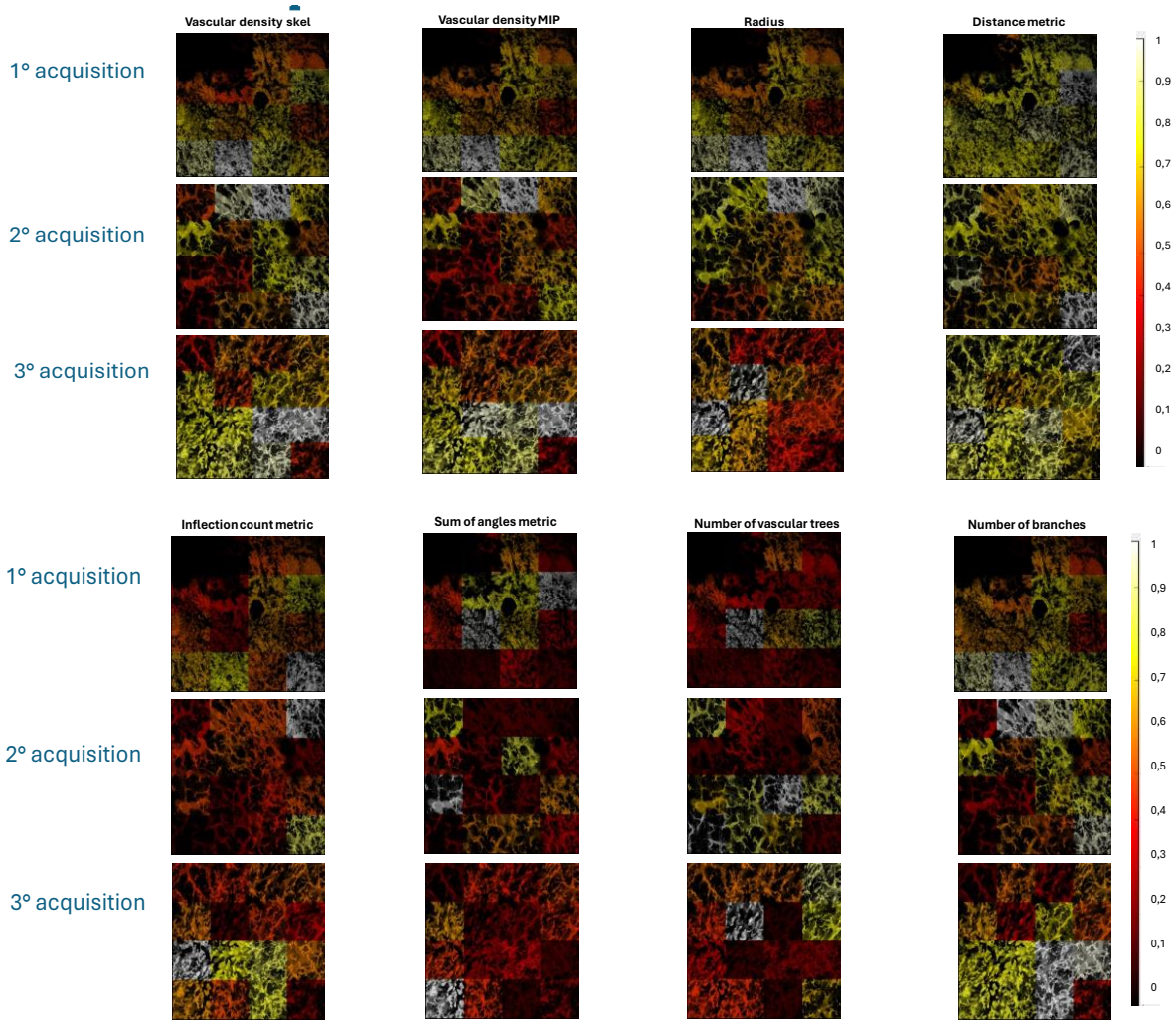

Figure 3.2: Heatmap without Roi's overlap and min-max scaling normalization.

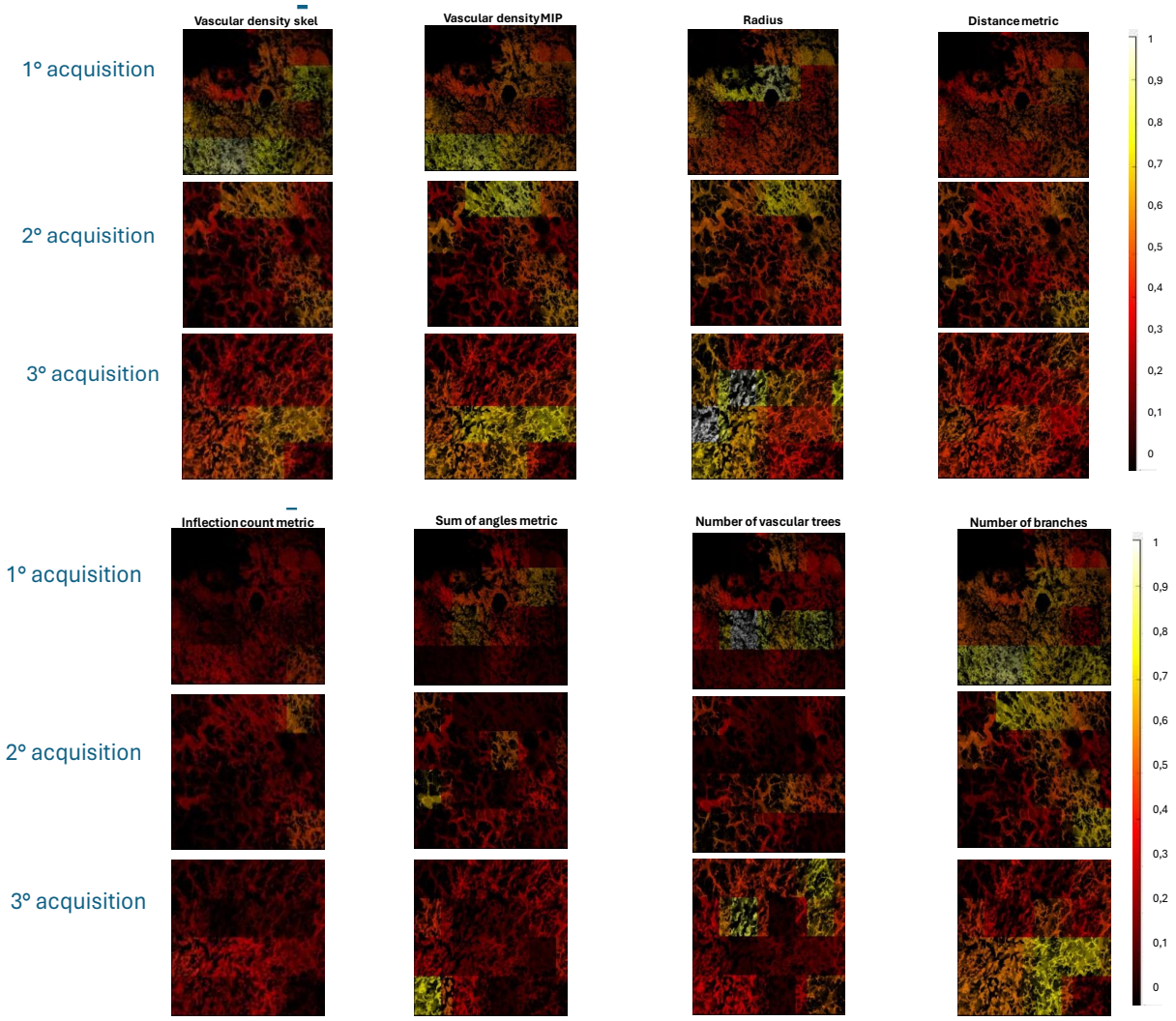

Figure 3.3: Heatmap with Roi's overlap and patient-based normalization.

.

3.Results

3.1 Lesion Analysis

3.1.1 Lesion-based qualitative analysis

In this subsection, the evolution of the OCTA images across different processing stages over time is examined. The lesion images are presented to visualize the morphological changes across the three acquisitions. A comparison of depth color coding allowing for a qualitative assessment of how the vascular structure and lesion morphology change over time. The images (Figs 3.4-3.7) primarily focus on the lesions of the first patient, used as an example, but the same qualitative comparison was conducted for all other lesions across patients. This qualitative analysis will be complemented by quantitative analysis to provide a comprehensive understanding of lesion evolution.

ST001- Lesion in position 1

1° acquisition

2° acquisition

3°acquisition

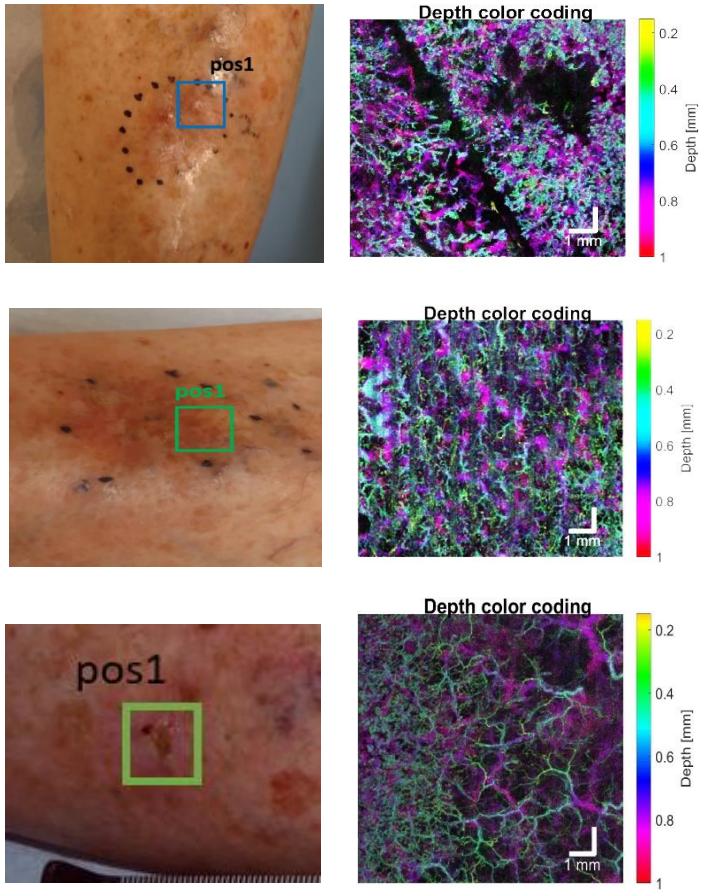

Figure 3.4: For each acquisition session, an image of the lesion in position 1 is shown alongside its corresponding depth color-coding map

ST001- Lesion in position 2

1° acquisition

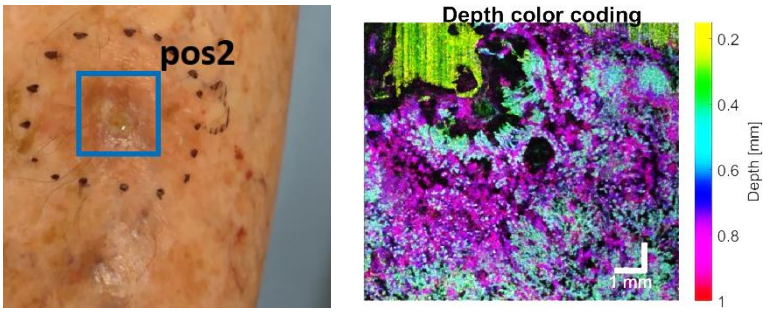

2° acquisition

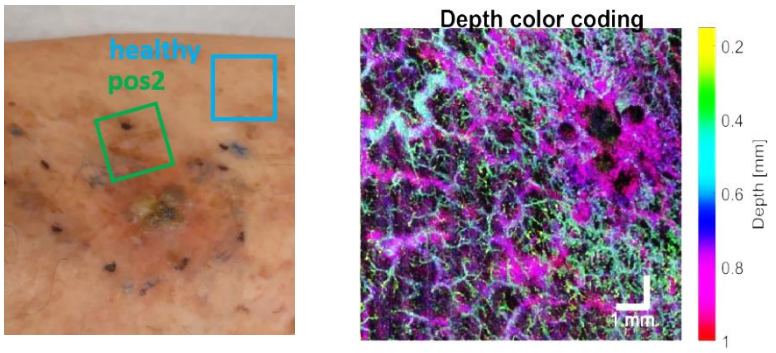

3°acquisition

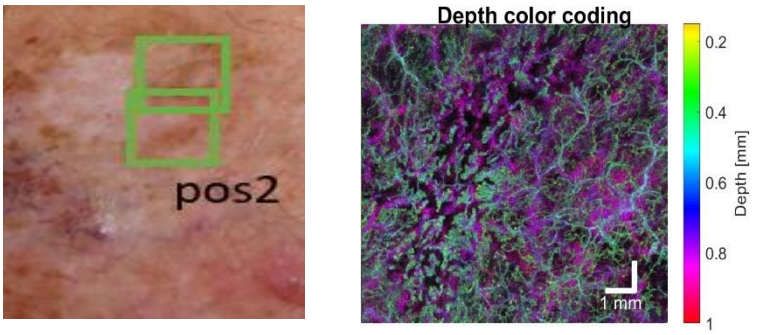

Figure 3.5: For each acquisition session, an image of the lesion in position 2 is shown alongside its corresponding depth color-coding map

ST001- Lesion in position 3

1° acquisition

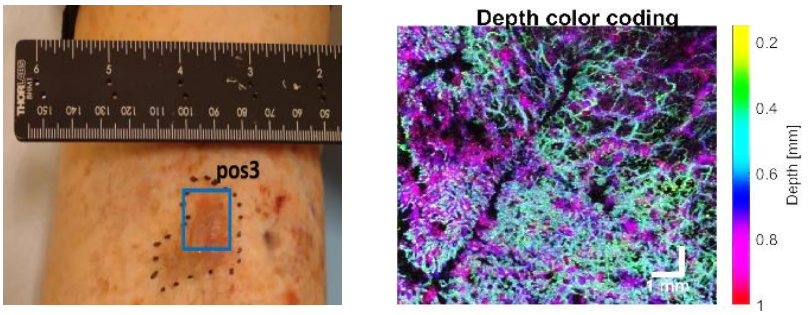

2° acquisition

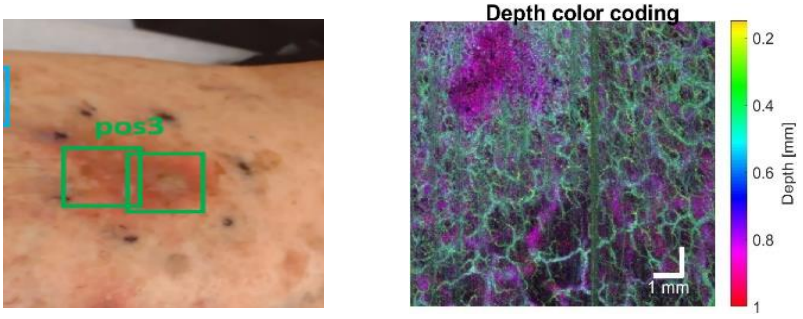

3°acquisition

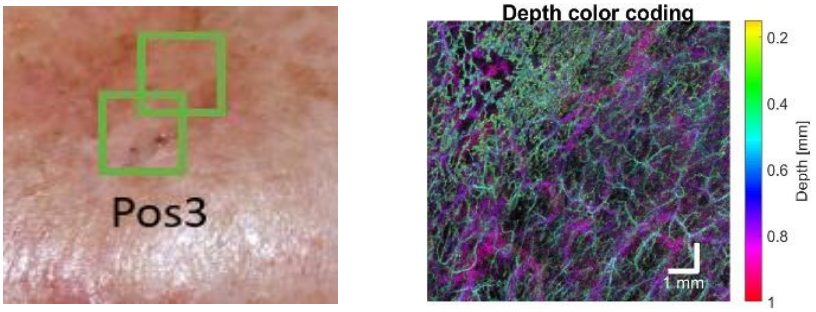

Figure 3.6: For each acquisition session, an image of the lesion in position 3 is shown alongside its corresponding depth color-coding map

ST001- Lesion in position 4

1° acquisition

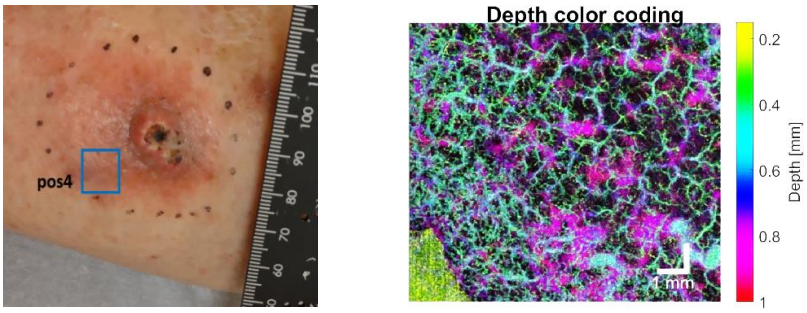

2° acquisition

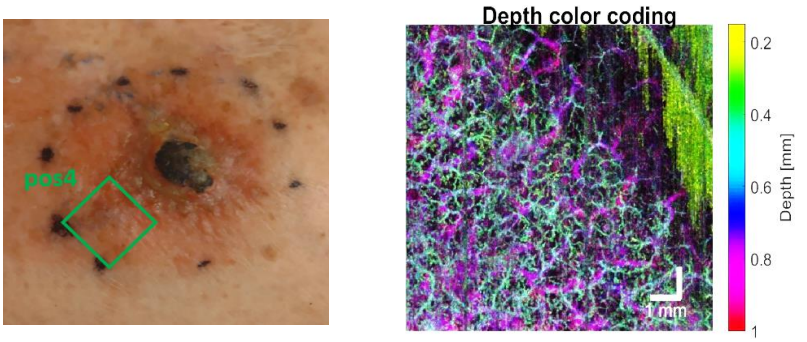

3°acquisition

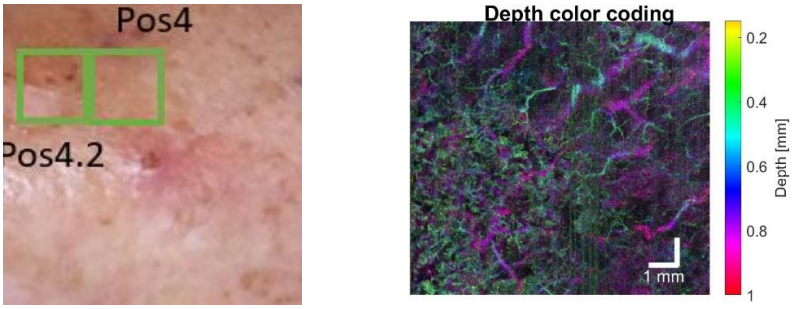

Figure 3.7: For each acquisition session, an image of the lesion in position 4 is shown alongside its corresponding depth color-coding map

3.1.2 Lesion-based quantitative analysis

In this subsection, graphs are presented showing the change in the maximum and average values of each parameter for every lesion in each patient, analyzed in the three acquisition sessions (Figs 3.8-3.11). The variations in the maximum values are represented in red on the graphs, while the changes in the average values are shown in blue.

These graphs show the temporal trend of each parameter, providing quantitative information on changes and progression of the lesions. Additionally, heatmaps corresponding to each parameter are presented, so that changes in results can be observed by color. The heatmaps were generated by normalizing the parameter matrices for each pixel to a range from 0 to 1. A patient-based normalization approach was used, with a 30% overlap of the ROIs.These graphical representations offer an immediate interpretation of the changes in the analyzed parameters, facilitating the understanding of the dynamics associated with the lesions over time. The graphs presented primarily illustrate the lesions of the first patient, but similar calculations were performed for all other patients.

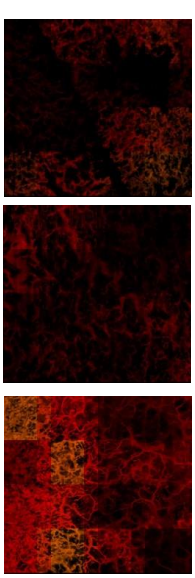

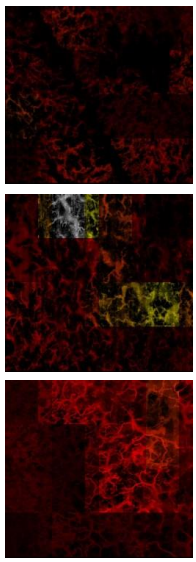

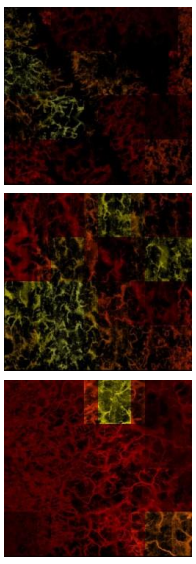

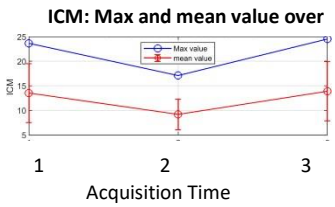

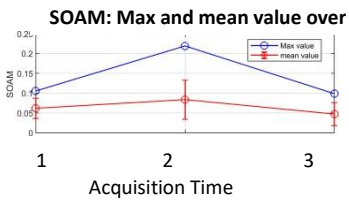

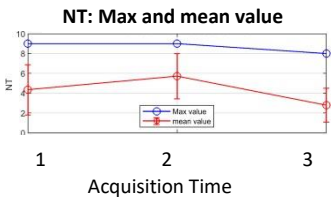

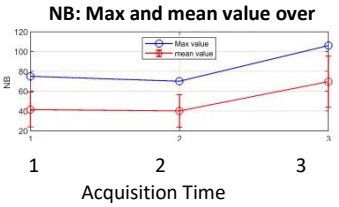

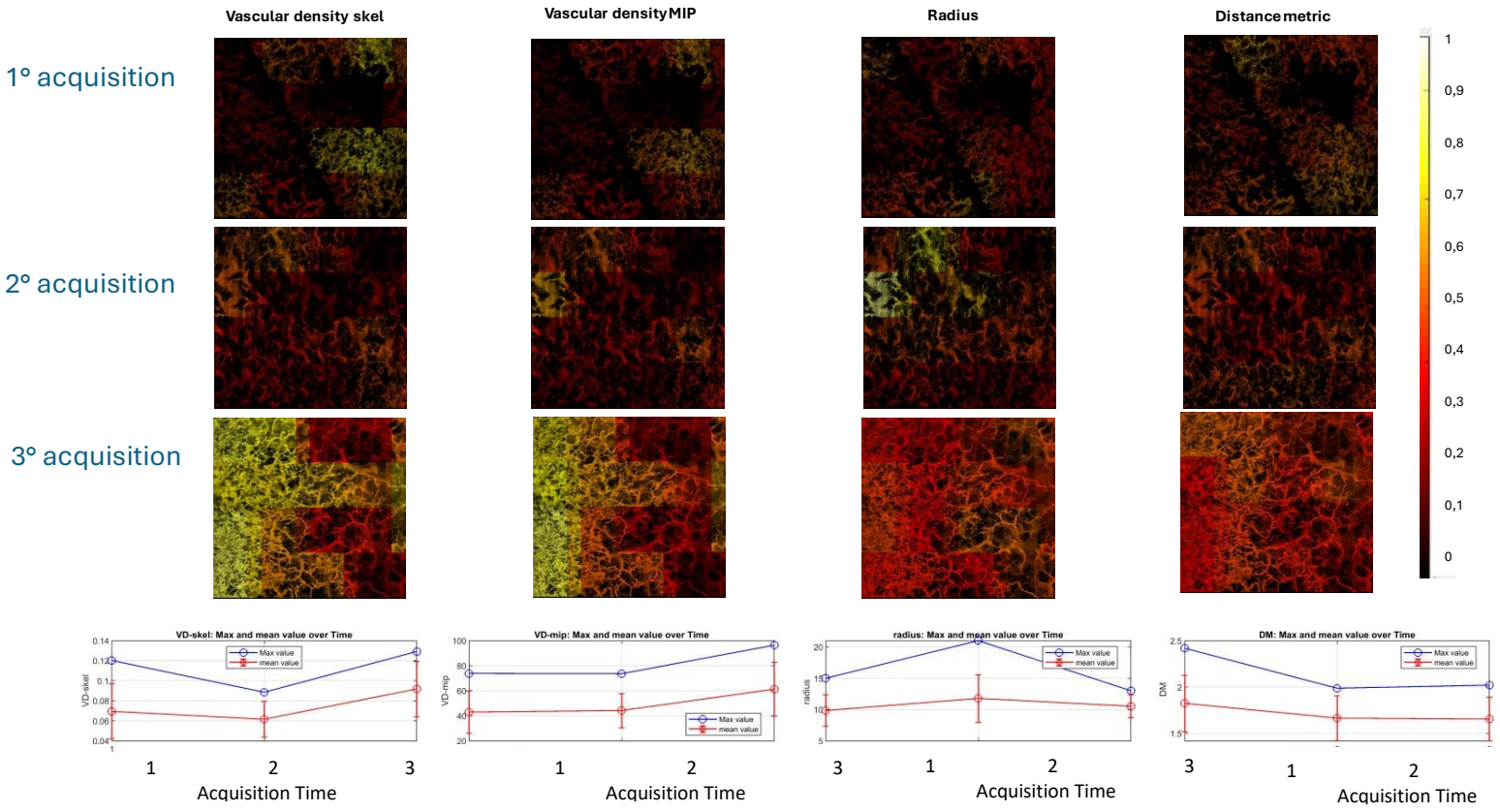

Figure 3.8: Visualization of vascular parameters of lesion in position 1, including vessel density, vessel radius, distance metric, number of trees, number of branches, inflection count metric, and angle sum metric. For each parameter, heat maps illustrate the changes between the three acquisitions, while the graphs below show the changes in maximum (blue) and average(red) values between the three acquisition sessions.

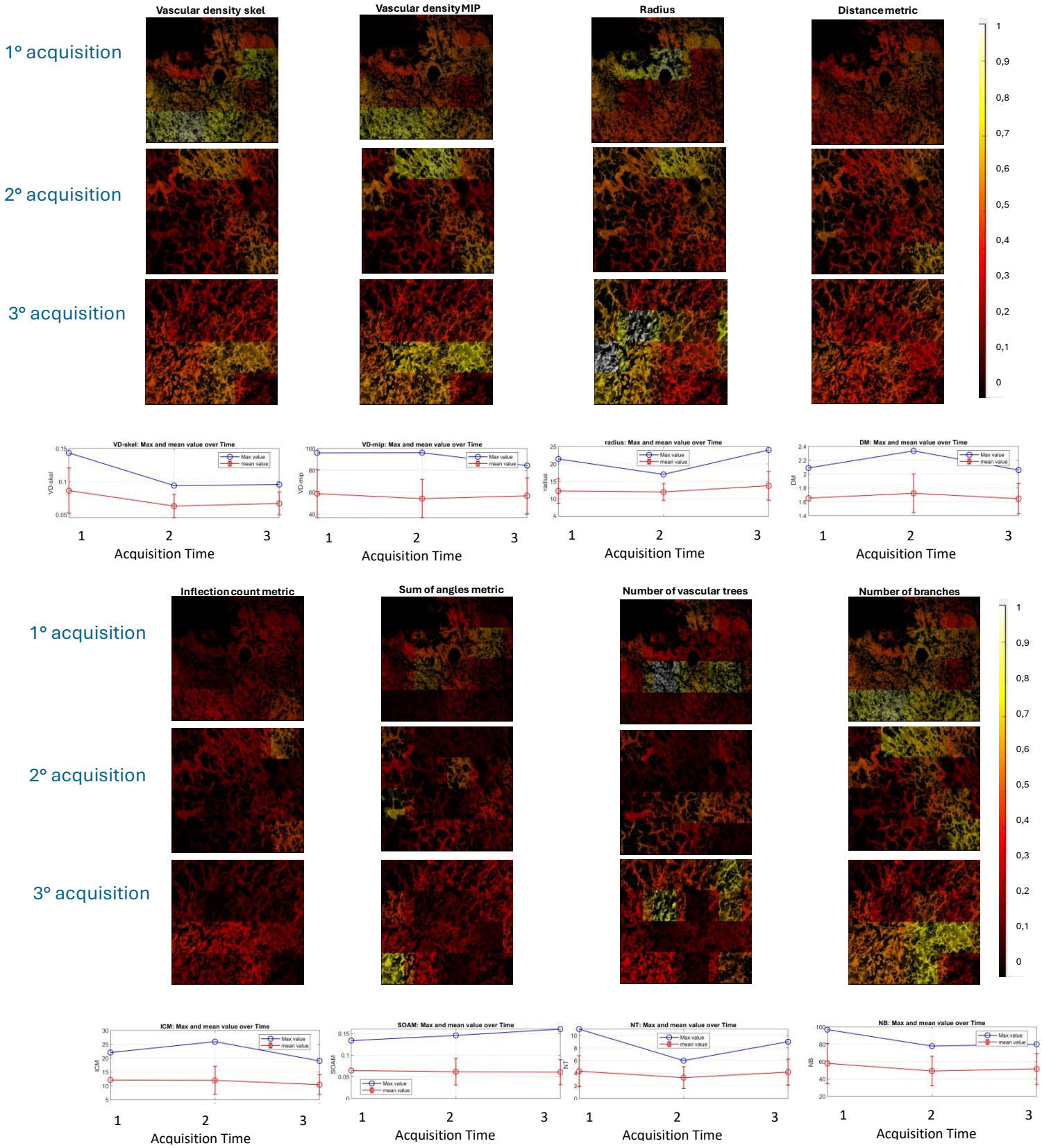

Figure 3.9: Visualization of vascular parameters of lesion in position 2, including vessel density, vessel radius, distance metric, number of trees, number of branches, inflection count metric, and angle sum metric. For each parameter, heat maps illustrate the changes between the three acquisitions, while the graphs below show the changes in maximum (blue) and average(red) values between the three acquisition sessions.

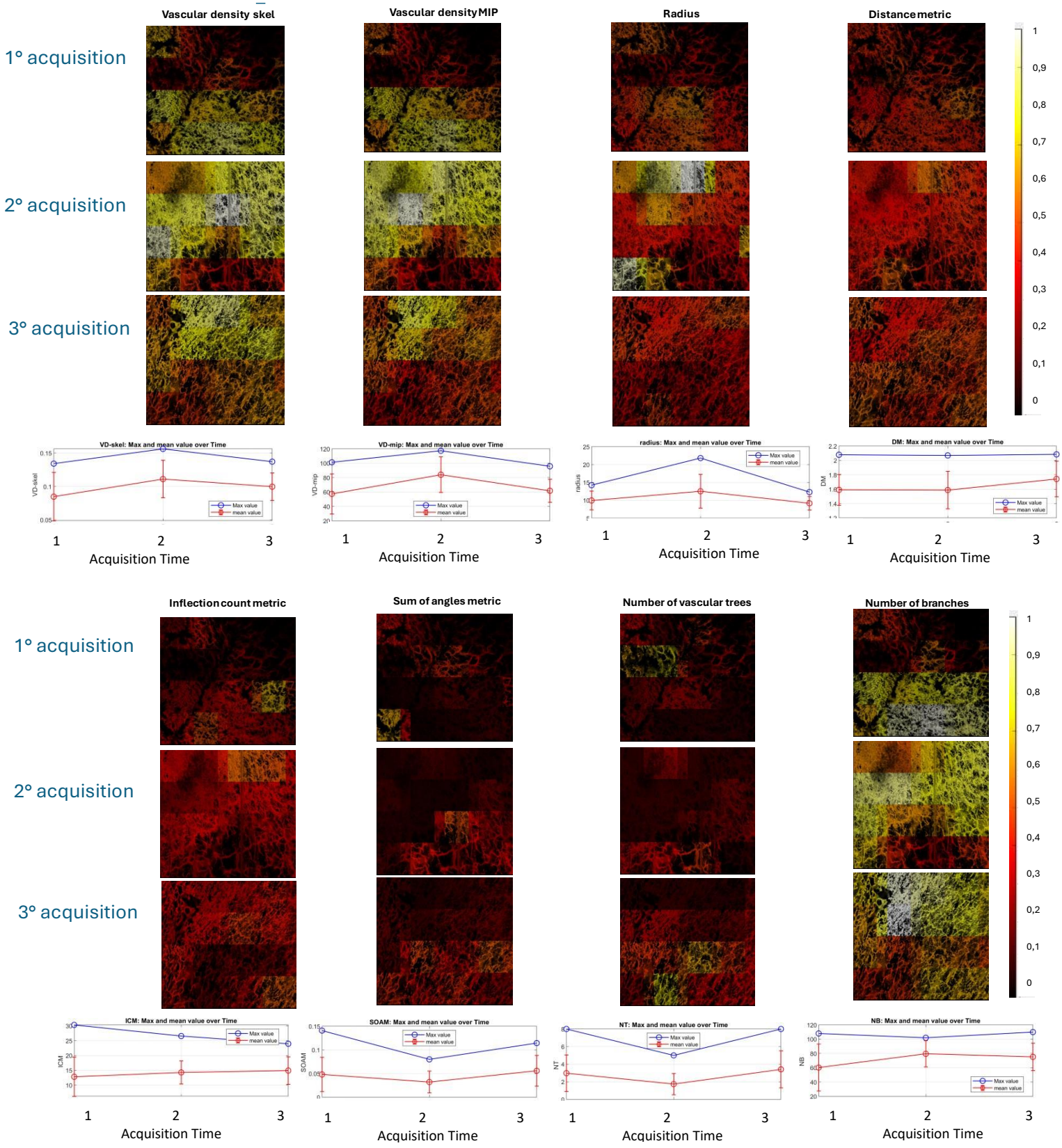

Figure 3.10: Visualization of vascular parameters of lesion in position 3, including vessel density, vessel radius, distance metric, number of trees, number of branches, inflection count metric, and angle sum metric. For each parameter, heat maps illustrate the changes between the three acquisitions, while the graphs below show the changes in maximum(blue) and average(red) values between the three acquisition sessions.

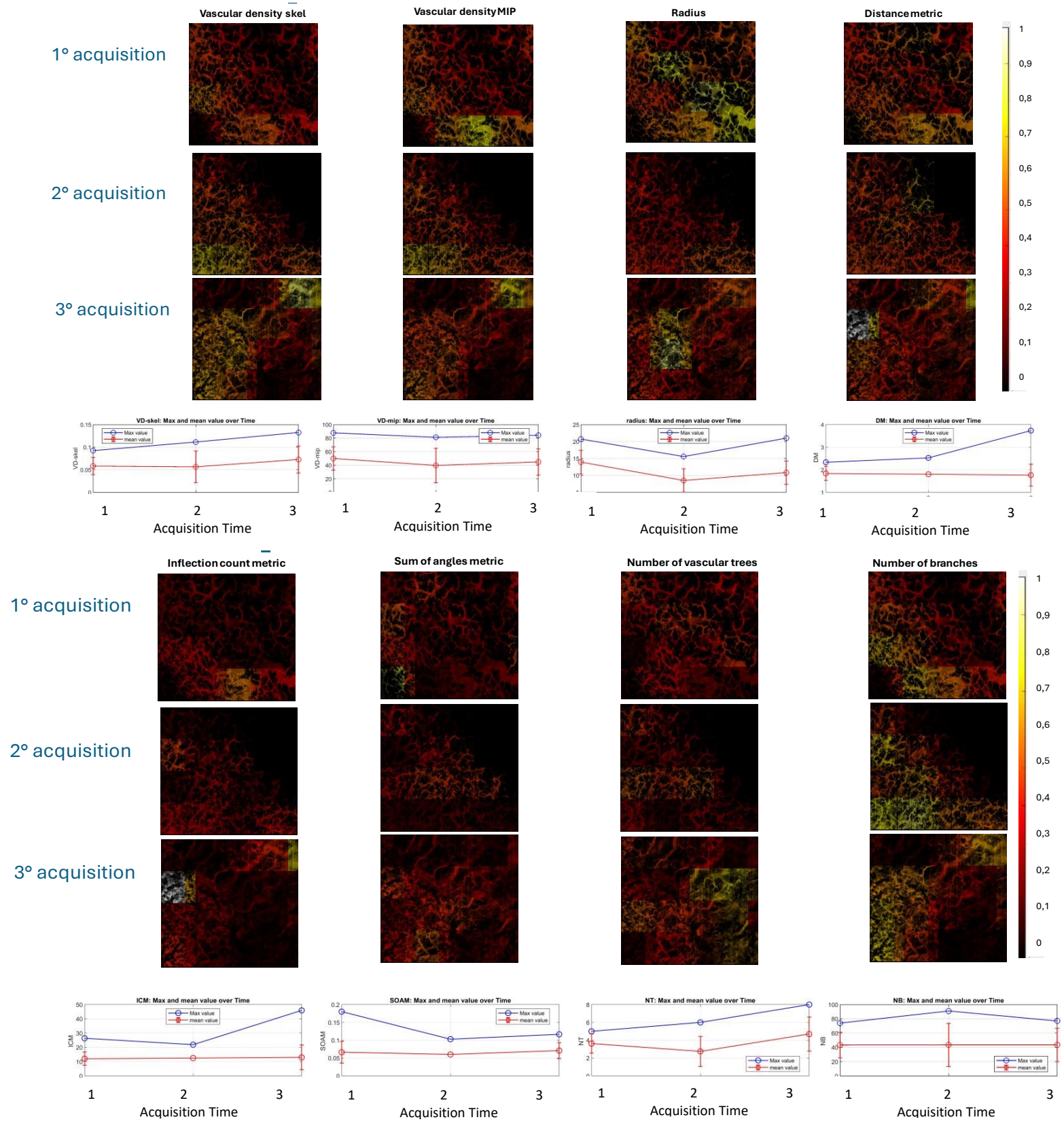

Figure 3.11: Visualization of vascular parameters of lesion in position 4, including vessel density, vessel radius, distance metric, number of trees, number of branches, inflection count metric, and angle sum metric. For each parameter, heat maps illustrate the changes between the three acquisitions, while the graphs below show the changes in maximum(blue) and average(red) values between the three acquisition sessions.

3.2 Healthy vs lesions

The results of the comparison between the various parameters extracted from healthy skin and the lesion for each patient and each acquisition session are presented through boxplots in Fig 3.12. For each parameter, the 16 values calculated within individual ROIs are compared between healthy skin and the lesion. Additionally, a t-test was used to view whether there are significant differences between the two conditions, considering the p-value: if less than 0.05, the difference is significant, while higher values indicate a nonsignificant difference.

The comparison between healthy skin and lesions for each patient is shown in Figure 3.12 for the first acquisition. This procedure was also repeated for the second and third acquisitions; however, the corresponding boxplots are not shown here.

For the first patient (Fig 3.12A), there is a significant difference in vascular density between all lesions and healthy skin, with a p-value below 0.05. The lesions show increased vascular density, which is consistent with findings reported in the literature, as discussed in the section 4.1.Vessel radius is also significantly smaller in healthy skin, with the most notable difference between lesion in position 4 and healthy skin (p-value of 8.42×10^{-8}). Number of trees does not show significant differences, as indicated by p-values above 0.05. In contrast, he number of branches shows significant differences, with lower values for healthy skin. Regarding the parameters related to tortuosity, the most significant differences are observed for ICM, which is significantly lower in healthy skin than in lesions, with p-values ranging from 10^{-2} to 10^{-3}. Additionally, the distance metric of lesions at positions 1 and 4 is significantly greater than in healthy skin.

For the second patient, as shown in Fig 3.12B, the lesion shows significantly higher values for vascular density, radius, and the number of branches.

In the third patient, as illustrated in Fig 3.12C, lesion in position 1 has significantly increased vascular parameters, particularly vessel radius and density, both with p-values below 0.05.

For the fourth patient (Fig 3.12D) , the radius always remains significantly lower than the lesion at position 1.The rest of the parameters are not statistically higher than the healthy skin.

Finally, in the fifth patient, as presented in Fig 3.12E, vascular density is statistically higher in all lesions compared to healthy skin, along with the number of branches and ICM.

(A)

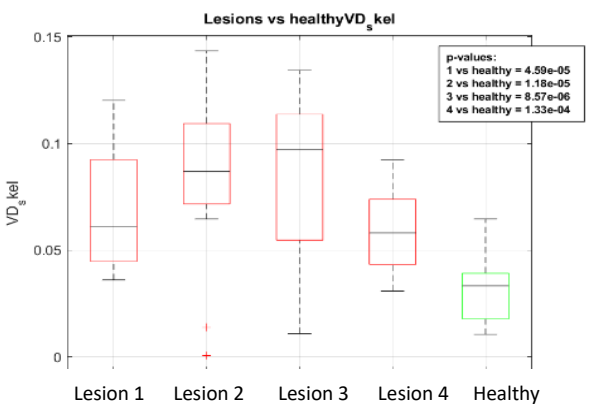

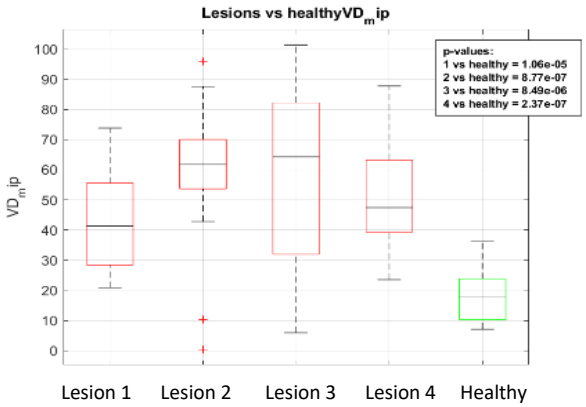

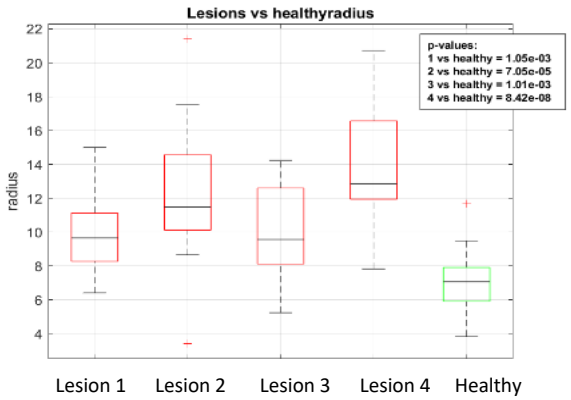

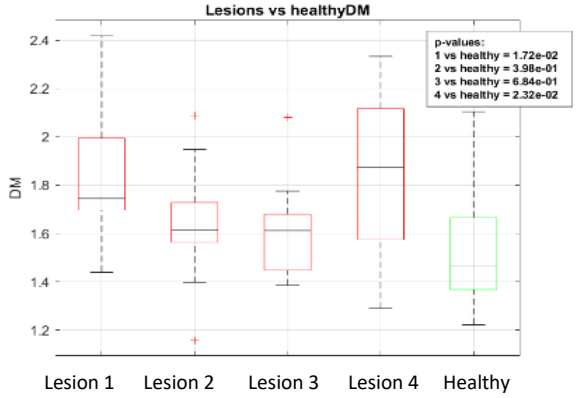

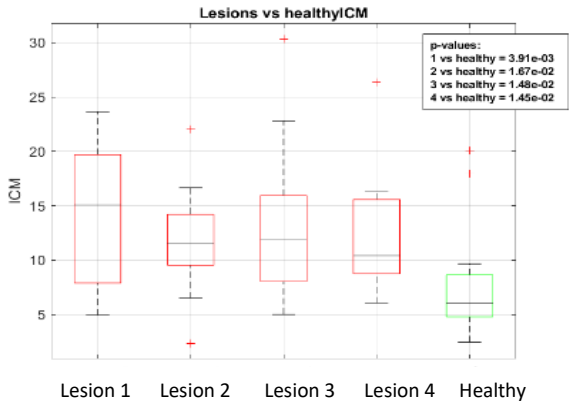

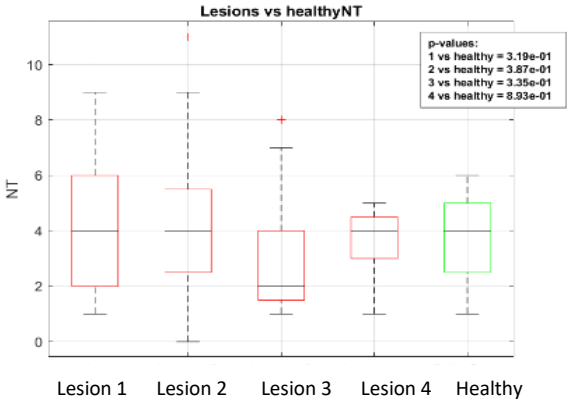

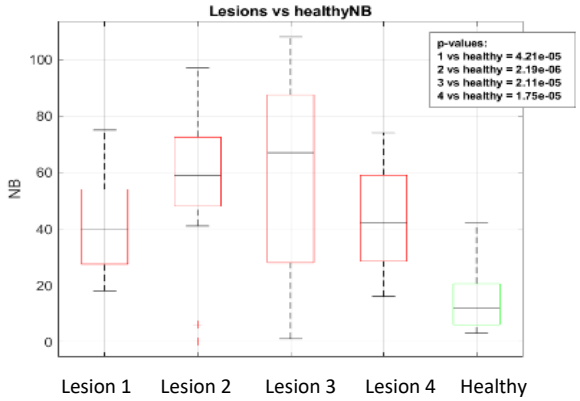

(B)

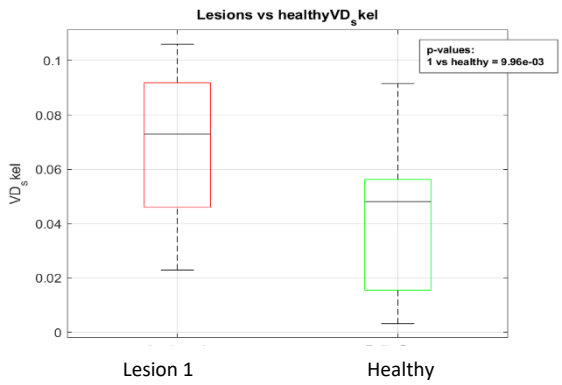
Lesions vs healthyVD_skel
p-values:
1 vs healthy = 9.96e-03
VD_skel
Lesion 1
Healthy

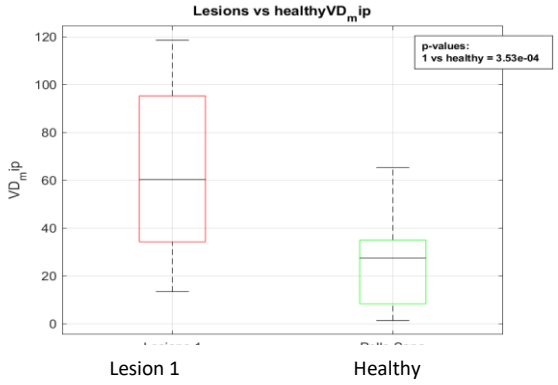
Lesions vs healthyVD_mip
p-values:
1 vs healthy = 3.53e-04
VD_mip
Lesion 1
Healthy

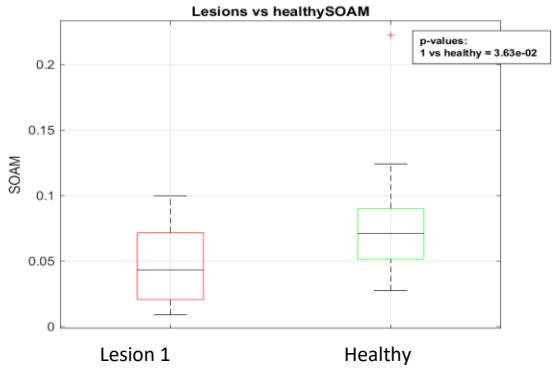
Lesions vs healthySOAM
p-values:
1 vs healthy = 3.63e-02
SOAM
Lesion 1
Healthy

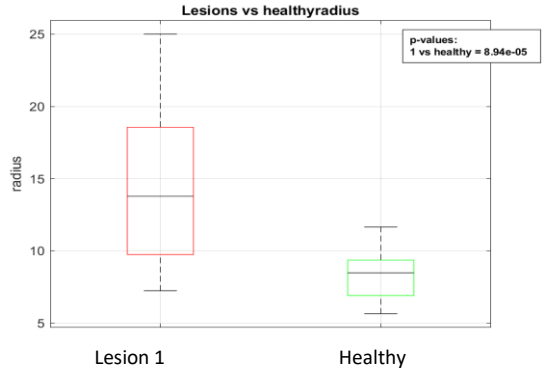
Lesions vs healthyradius
p-values:
1 vs healthy = 8.94e-05
radius
Lesion 1
Healthy

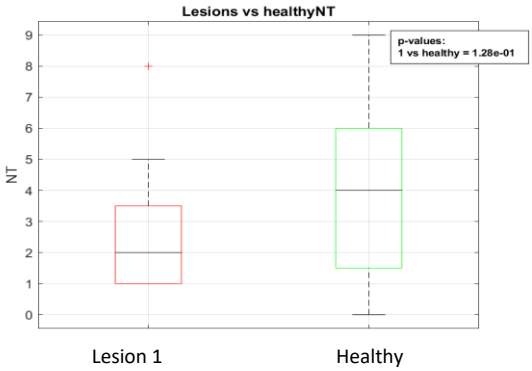
Lesions vs healthyNT
p-values:
1 vs healthy = 1.28e-01
NT
Lesion 1
Healthy

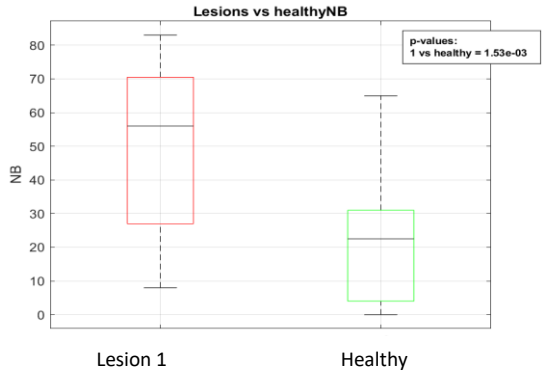
Lesions vs healthyNB
p-values:
1 vs healthy = 1.53e-03
NB
Lesion 1
Healthy

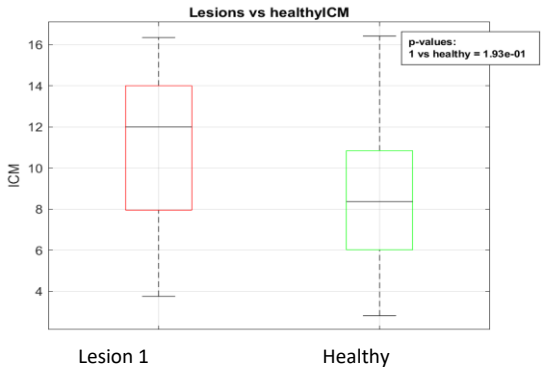
Lesions vs healthyICM
p-values:
1 vs healthy = 1.93e-01
ICM
Lesion 1
Healthy

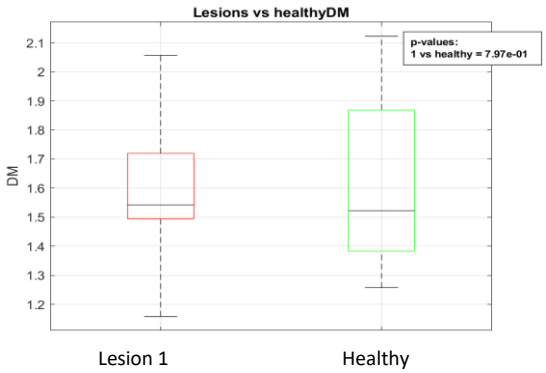
Lesions vs healthyDM
p-values:
1 vs healthy = 7.97e-01
DM
Lesion 1
Healthy

(C)

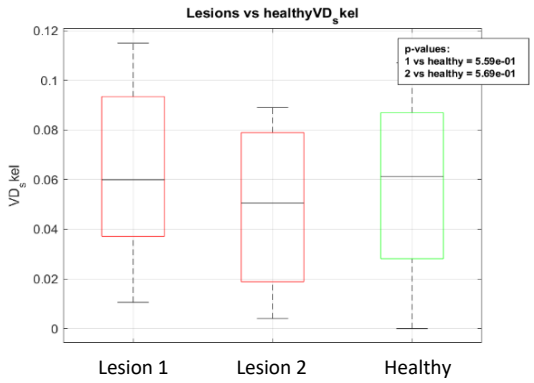
Lesions vs healthyVD_s kel
p-values:
1 vs healthy = 5.59e-01
2 vs healthy = 5.69e-01
VD_s kel
Lesion 1
Lesion 2
Healthy

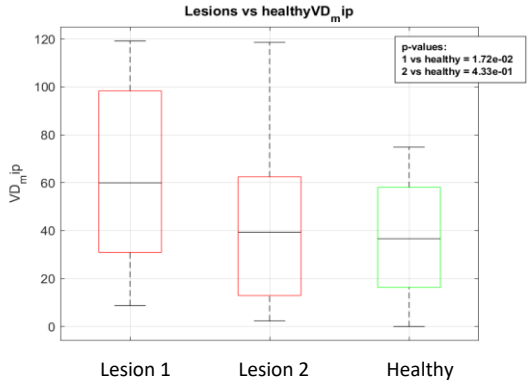
Lesions vs healthyVD_m ip
p-values:
1 vs healthy = 1.72e-02
2 vs healthy = 4.33e-01
VD_m ip
Lesion 1
Lesion 2
Healthy

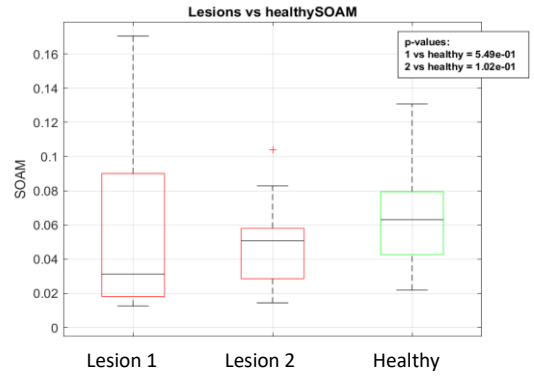
Lesions vs healthySOAM
p-values:
1 vs healthy = 5.49e-01
2 vs healthy = 1.02e-01
SOAM
Lesion 1
Lesion 2
Healthy

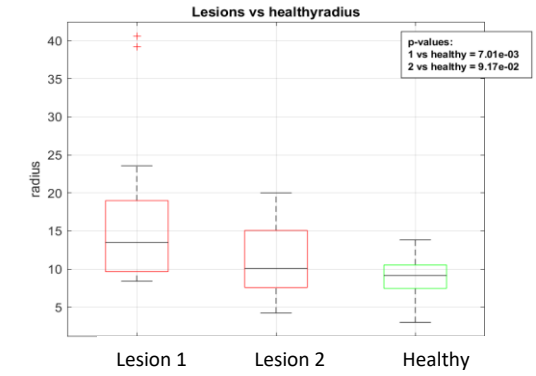
Lesions vs healthyradius
p-values:
1 vs healthy = 7.01e-03
2 vs healthy = 9.17e-02
radius
Lesion 1
Lesion 2
Healthy

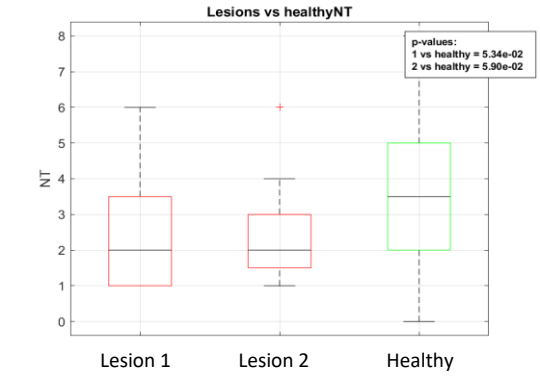
Lesions vs healthyNT
p-values:
1 vs healthy = 5.34e-02
2 vs healthy = 5.90e-02
NT
Lesion 1
Lesion 2
Healthy

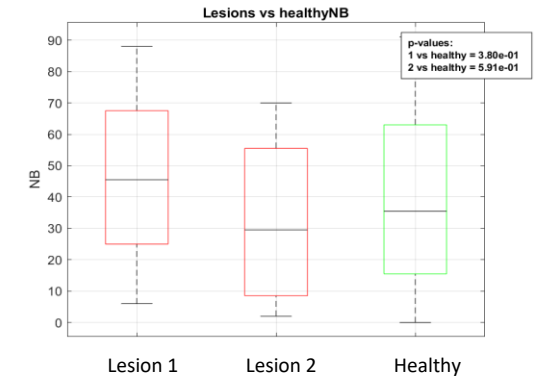
Lesions vs healthyNB
p-values:
1 vs healthy = 3.80e-01
2 vs healthy = 5.91e-01
NB
Lesion 1
Lesion 2
Healthy

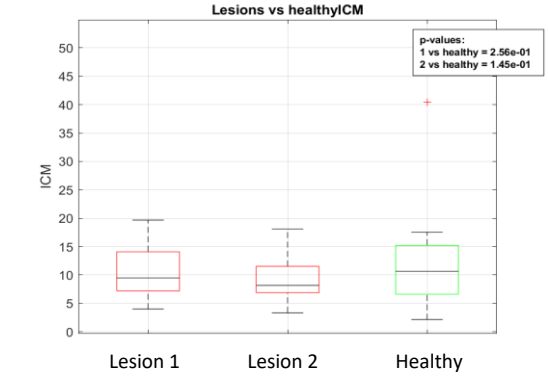
Lesions vs healthyICM
p-values:
1 vs healthy = 2.56e-01
2 vs healthy = 1.45e-01
ICM
Lesion 1
Lesion 2
Healthy

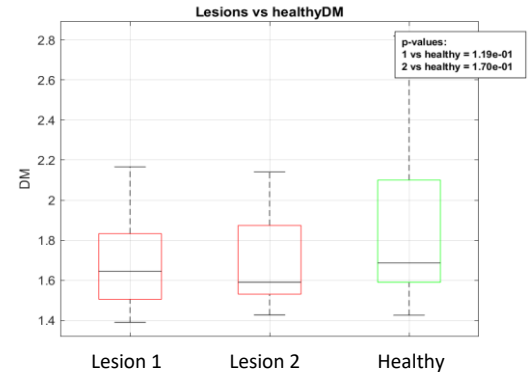
Lesions vs healthyDM
p-values:
1 vs healthy = 1.19e-01
2 vs healthy = 1.70e-01
DM
Lesion 1
Lesion 2
Healthy

(D)

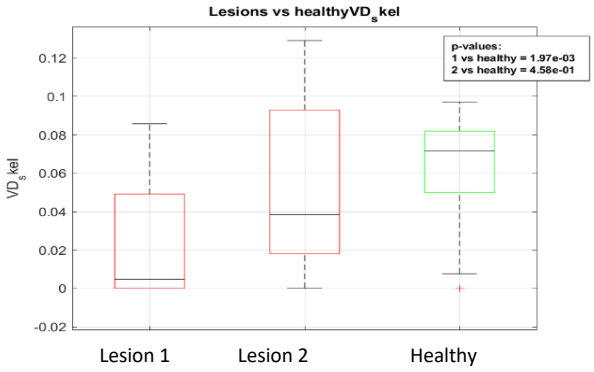
Lesions vs healthyVD_s_kel
p-values:
1 vs healthy = 1.97e-03
2 vs healthy = 4.58e-01
VD_s_kel
0.12
0.1
0.08
0.06
0.04
0.02
0
-0.02
Lesion 1
Lesion 2
Healthy

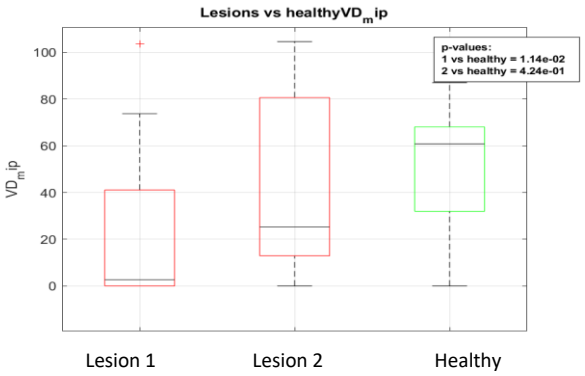
Lesions vs healthyVD_m_ip
p-values:
1 vs healthy = 1.14e-02
2 vs healthy = 4.24e-01
VD_m_ip
100
80
60
40
20
0
Lesion 1
Lesion 2
Healthy

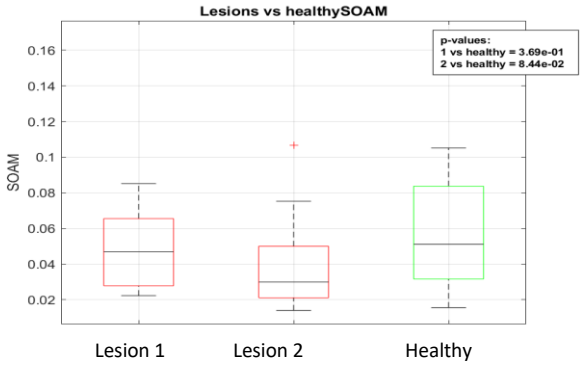
Lesions vs healthySOAM
p-values:
1 vs healthy = 3.69e-01
2 vs healthy = 8.44e-02
SOAM
0.16
0.14
0.12
0.1
0.08
0.06
0.04
0.02
Lesion 1
Lesion 2
Healthy

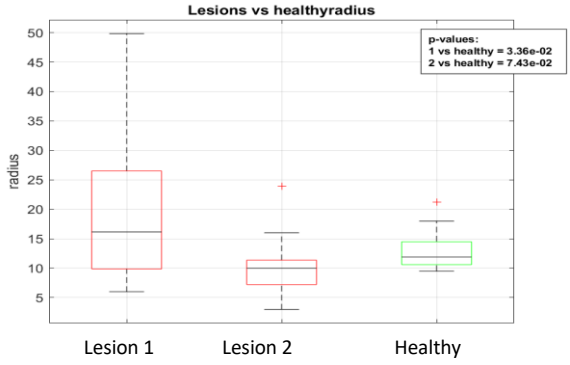
Lesions vs healthyradius
p-values:
1 vs healthy = 3.36e-02
2 vs healthy = 7.43e-02
radius
50
45
40
35
30
25
20
15
10
5
Lesion 1
Lesion 2
Healthy

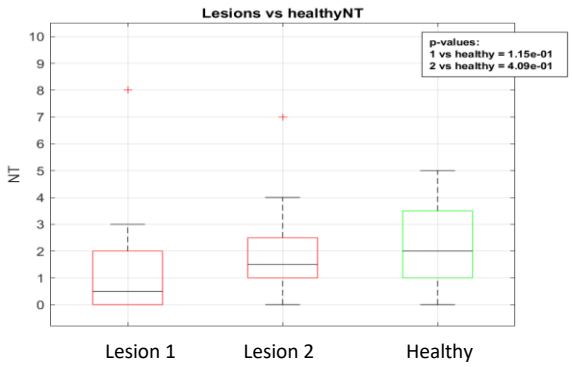
Lesions vs healthyNT
p-values:
1 vs healthy = 1.15e-01
2 vs healthy = 4.09e-01
NT
10
9
8
7
6
5
4
3
2
1
0
Lesion 1
Lesion 2
Healthy

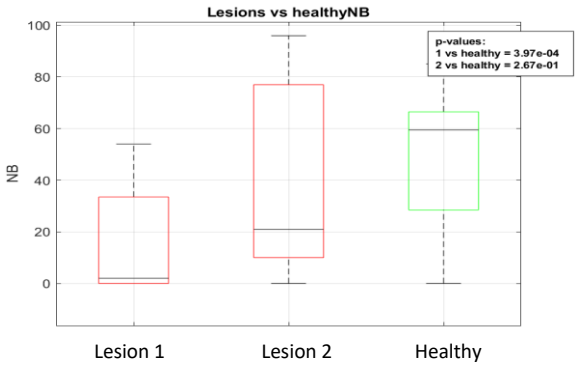
Lesions vs healthyNB
p-values:
1 vs healthy = 3.97e-04
2 vs healthy = 2.67e-01
NB
100
80
60
40
20
0
Lesion 1
Lesion 2
Healthy

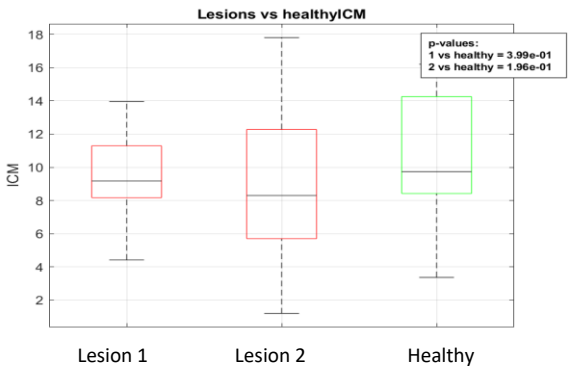
Lesions vs healthyICM
p-values:
1 vs healthy = 3.99e-01
2 vs healthy = 1.96e-01
ICM
18
16
14
12
10
8
6
4
2
Lesion 1
Lesion 2
Healthy

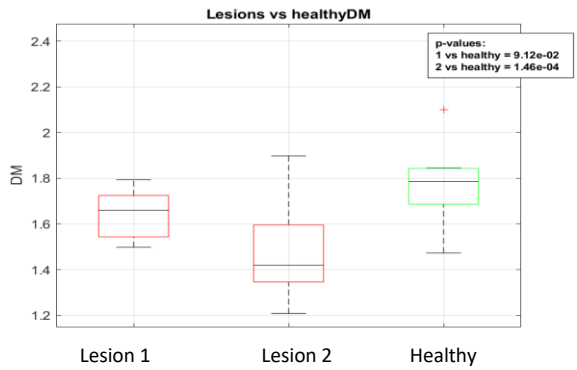
Lesions vs healthyDM
p-values:
1 vs healthy = 9.12e-02
2 vs healthy = 1.46e-04
DM
2.4
2.2
2
1.8
1.6
1.4
1.2
Lesion 1
Lesion 2
Healthy

(E)

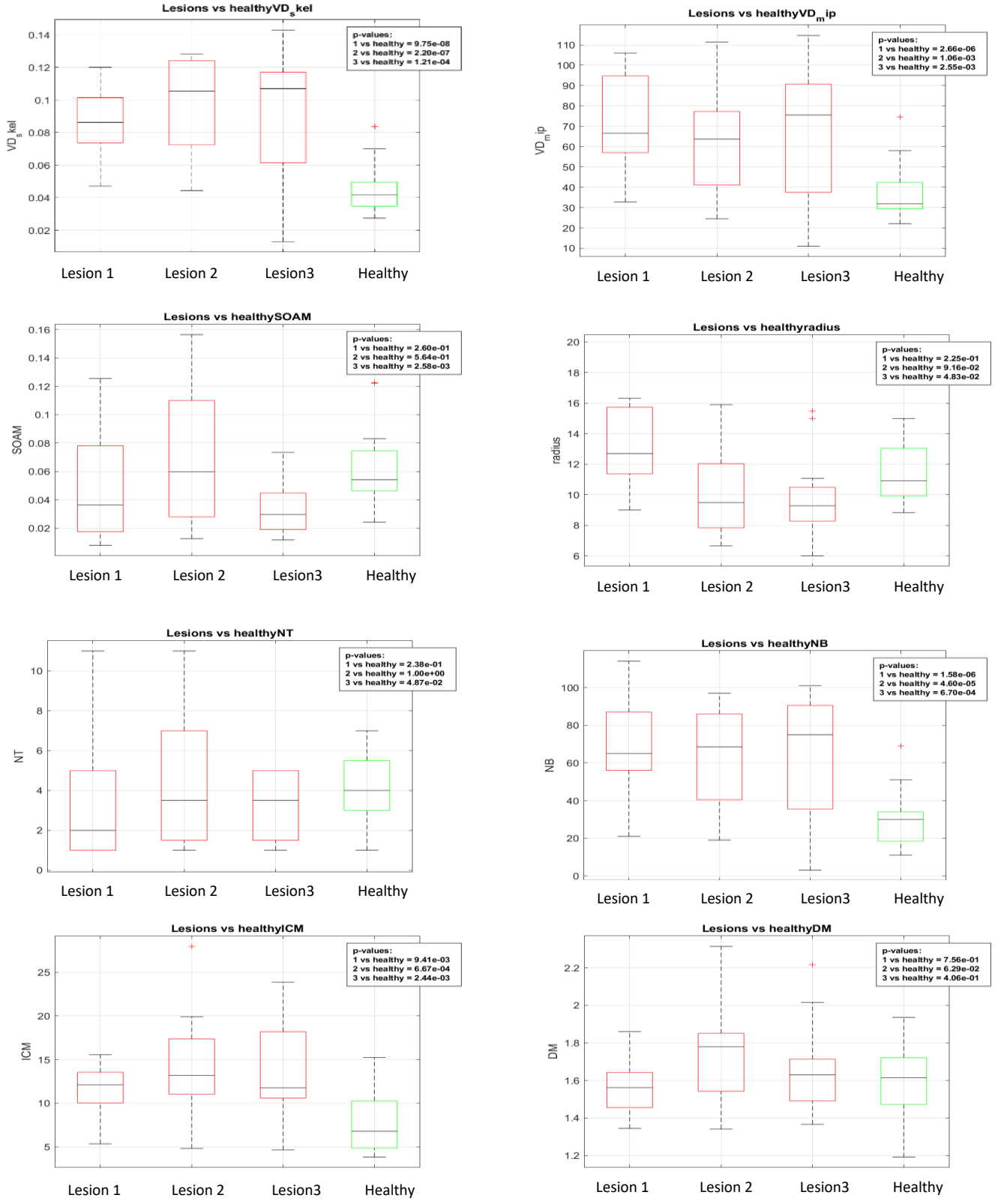

Figure 3.12: Graphs show the parameters of each lesion compared to those of healthy skin for patiens ST001 (A), ST002(B) , ST003(C) , ST004(D), ST005(E). The red boxplots represent the lesion parameters, while the green boxplots represent the parameters of healthy skin.

3.3 Dataset-based quantitative analysis

This section summarizes the results, showing how each parameter varies across all lesions for all patients over the three time-point acquisitions, using boxplots to observe changes over time, as shown in Figs 3.13-3.19. In addition, a green boxplot was included to represent the parameters for healthy tissue across all acquisitions, enabling a comparison between the lesions and healthy skin at each time point.

This approach facilitates comparisons across the three sessions, highlighting any statistically significant differences. For each parameter, the maximum value, mean value, and standard deviation were evaluated across the three acquisitions. Statistical tests were conducted between the first and second acquisitions, the second and third, and the first and third. The p-value was calculated to determine the significance of any differences, with a p-value below 0.05 indicating a statistically significant difference between acquisitions.

From the graphs, it can be observed that, when considering the entire dataset of the study, the parameter values show significant variations over time.

The maximum value of vascular density increases significantly between the second and third acquisitions ($p = 3.11 \times 10\text{-}^{2}$). In addition, across all time points, vascular density remains significantly higher in lesions compared to healthy skin (Fig 3.13).

The maximum and mean vessel radius decrease significantly between the second and third acquisitions ($p = 3.20 \times 10^{-2}$) , as shown in Fig 3.14.

Metric distance, both maximum and mean, does not vary significantly; however, the mean distance increases significantly between the second and third acquisitions ($p = 1.15 \times 10^{-2}$) , as illustrated in Fig 3.15.

The sum of angle metric (SOAM) does not show significant variation over time (Fig 3.16).

Inflection count metric (ICM) significantly increases between the second and third acquisitions for maximum values ($p = 1.46 \times 10^{-2}$). The average ICM remains continuously

higher in lesions compared to healthy skin throughout all acquisition phases, as highlighted in Fig 3.17.

No significant differences are found for the number of trees (NT) , as shown in Fig 3.18 .

However, the maximum number of branches (NB) significantly rises between the second and third acquisitions ($p = 4.08 \times 10^{-2}$). Comparison of the NB of lesions in the full dataset with that of healthy skin indicates that both the maximum and mean NB are significantly higher in lesions at all time points, while healthy skin consistently shows lower values (Fig 3.19) .

- **Vessel density:**

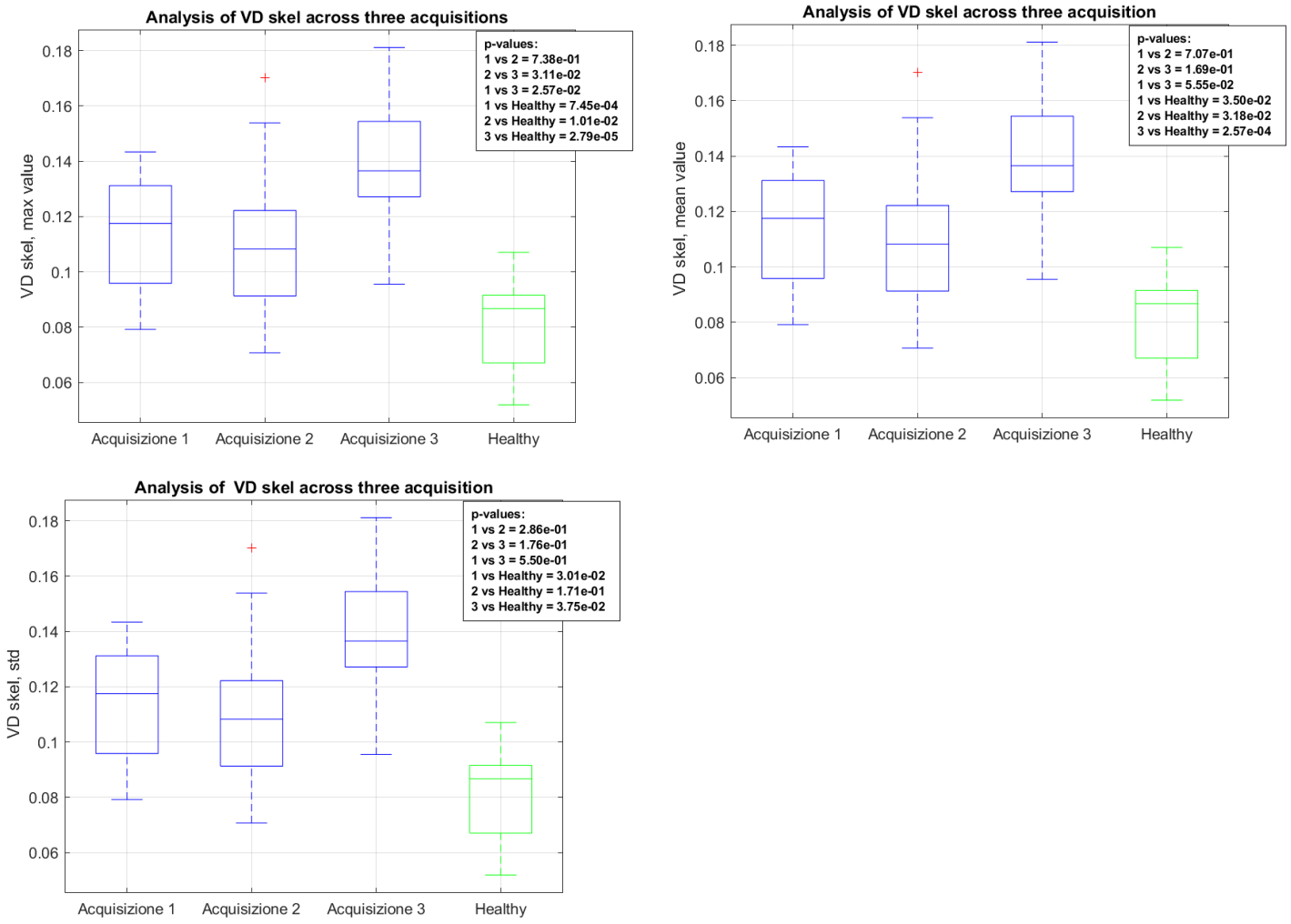

Figure 3.13: The three graphs represent the standard deviation, maximum value, and average value of vascular density for the entire dataset of lesion-related data across the first, second, and third acquisitions. The green boxplot indicate the corresponding parameter calculated for all acquisitions performed on healthy skin. . In each graph, the p-value for comparisons between the first and second, second and third, first and third acquisitions, as well as between each acquisition and healthy skin, is shown in the top right corner.

- **Radius :**

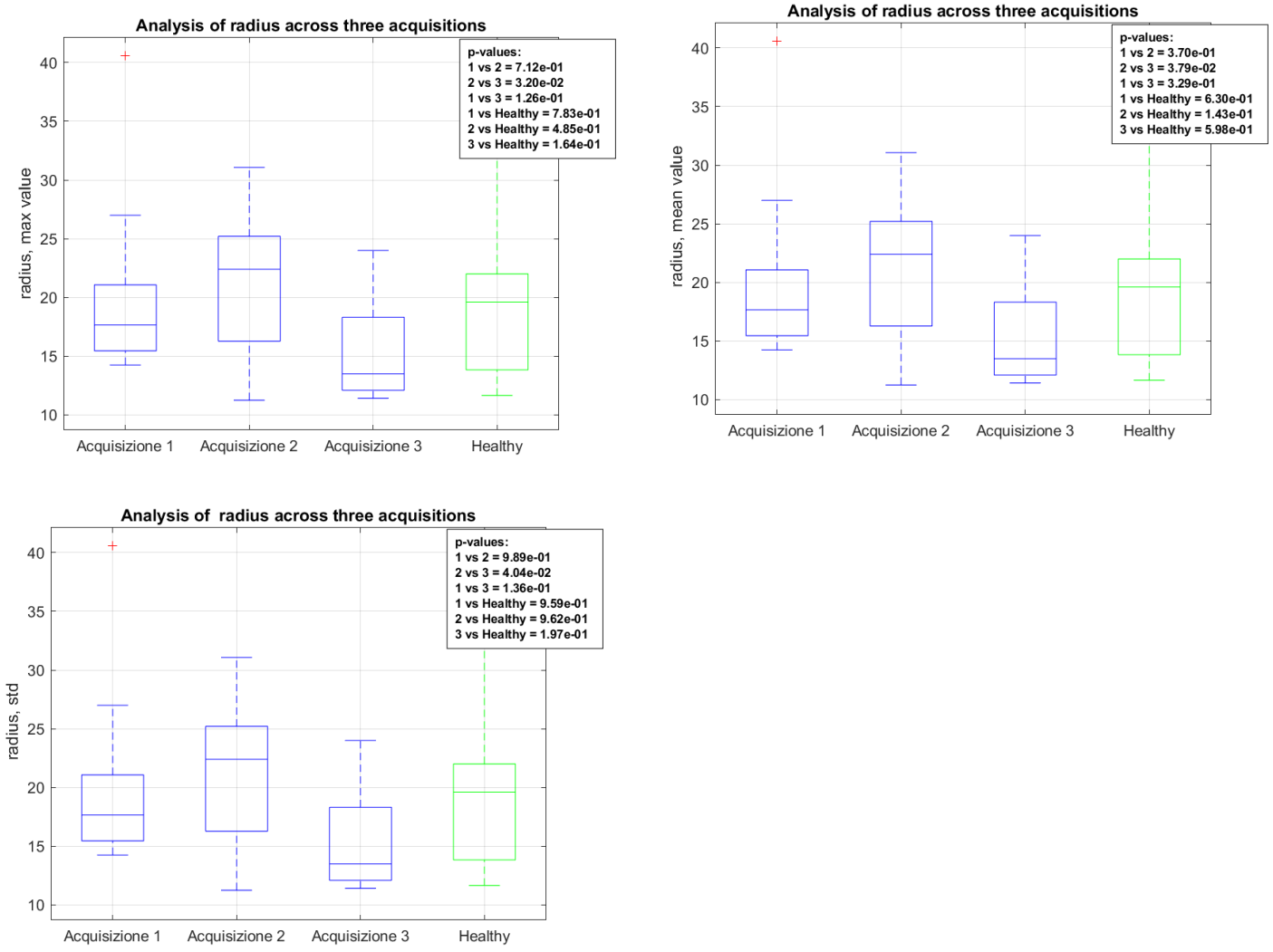

Figure 3.14: The three graphs represent the standard deviation, maximum value, and average value of vessel radius for the entire dataset of lesion-related data across the first, second, and third acquisitions. The green boxplot indicate the corresponding parameter calculated for all acquisitions performed on healthy skin. In each graph, the p-value for comparisons between the first and second, second and third, first and third acquisitions, as well as between each acquisition and healthy skin, is shown in the top right corner.

- **Distance metric**

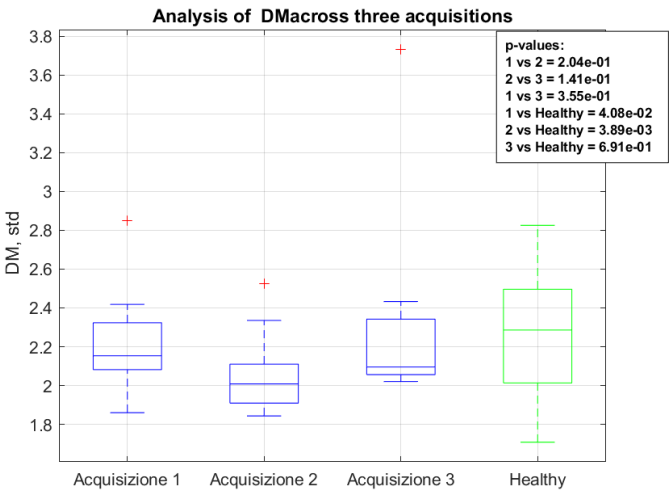

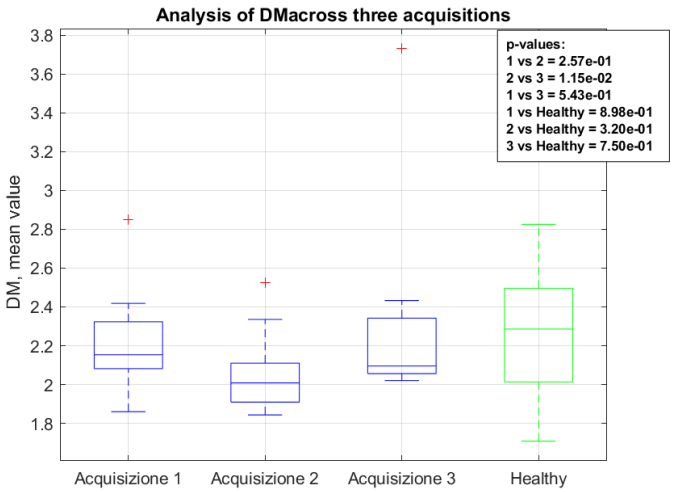

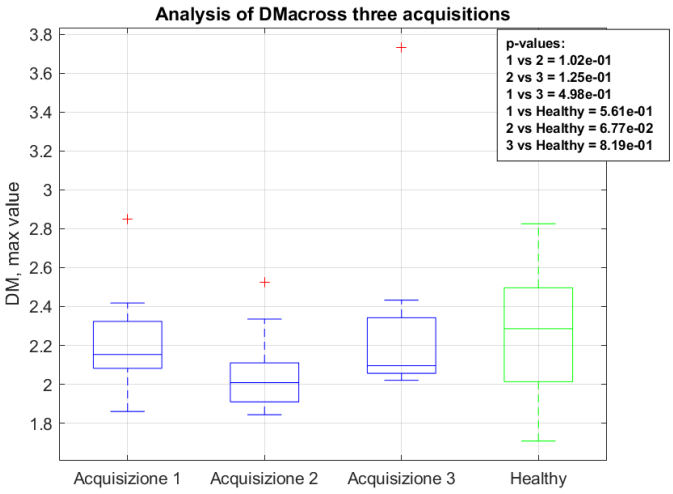

Figure 3.15: The three graphs represent the standard deviation, maximum value, and average value of distance metric for the entire dataset of lesion-related data across the first, second, and third acquisitions. The green boxplot indicate the corresponding parameter calculated for all acquisitions performed on healthy skin. In each graph, the p-value for comparisons between the first and second, second and third, first and third acquisitions, as well as between each acquisition and healthy skin, is shown in the top right corner.

- **Sum of angles metric**

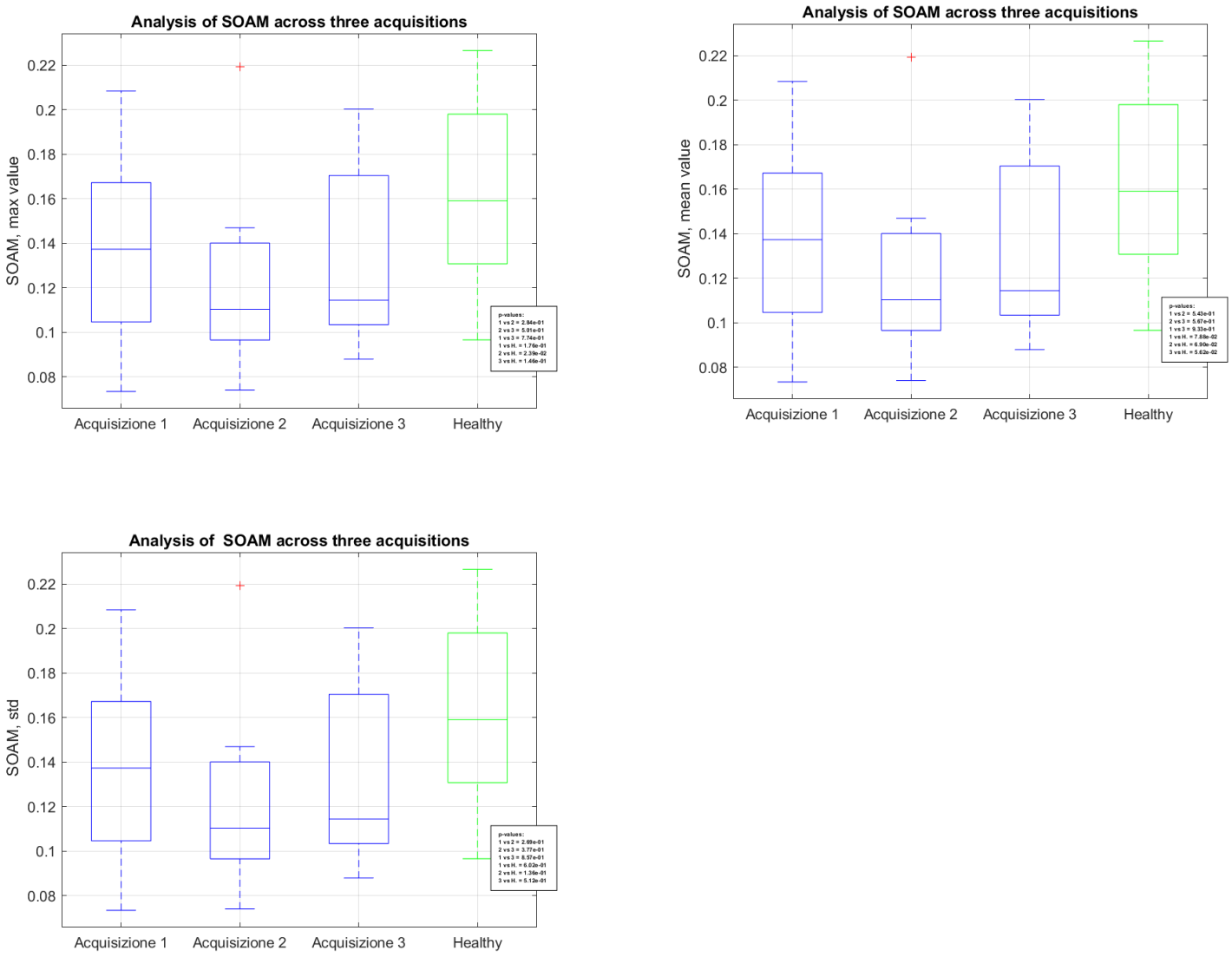

Figure 3.16: The three graphs represent the standard deviation, maximum value, and average value of sum of angles metric for the entire dataset of lesion-related data across the first, second, and third acquisitions. The green boxplot indicate the corresponding parameter calculated for all acquisitions performed on healthy skin. In each graph, the p-value for comparisons between the first and second, second and third, first and third acquisitions, as well as between each acquisition and healthy skin, is shown in the down right corner.

- **Inflection count metric**

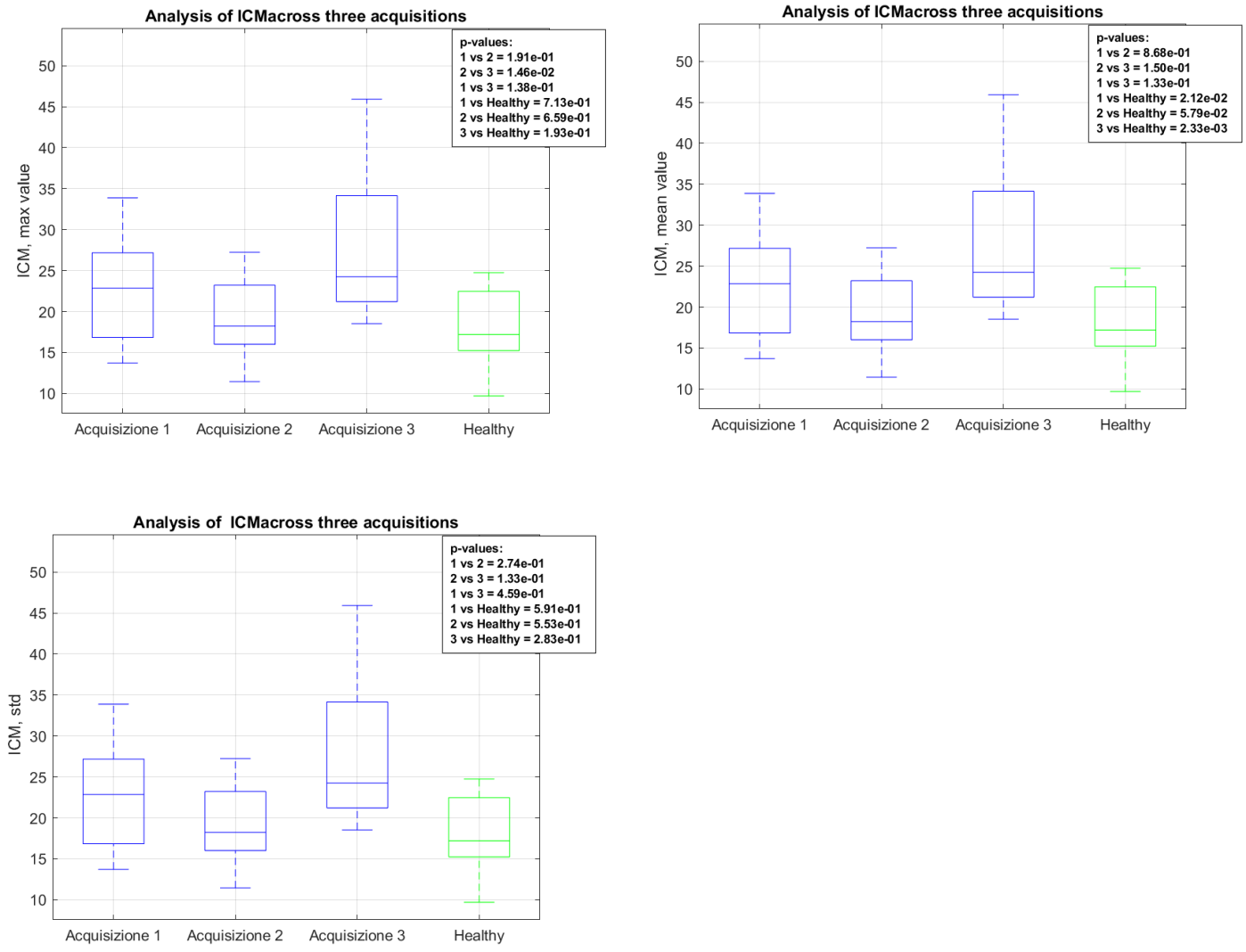

Figure 3.17: The three graphs represent the standard deviation, maximum value, and average value of inflection count metric for the entire dataset of lesion-related data across the first, second, and third acquisitions. The green boxplot indicate the corresponding parameter calculated for all acquisitions performed on healthy skin. In each graph, the p-value for comparisons between the first and second, second and third, first and third acquisitions, as well as between each acquisition and healthy skin, is shown in the top right corner.

- **Number of trees**

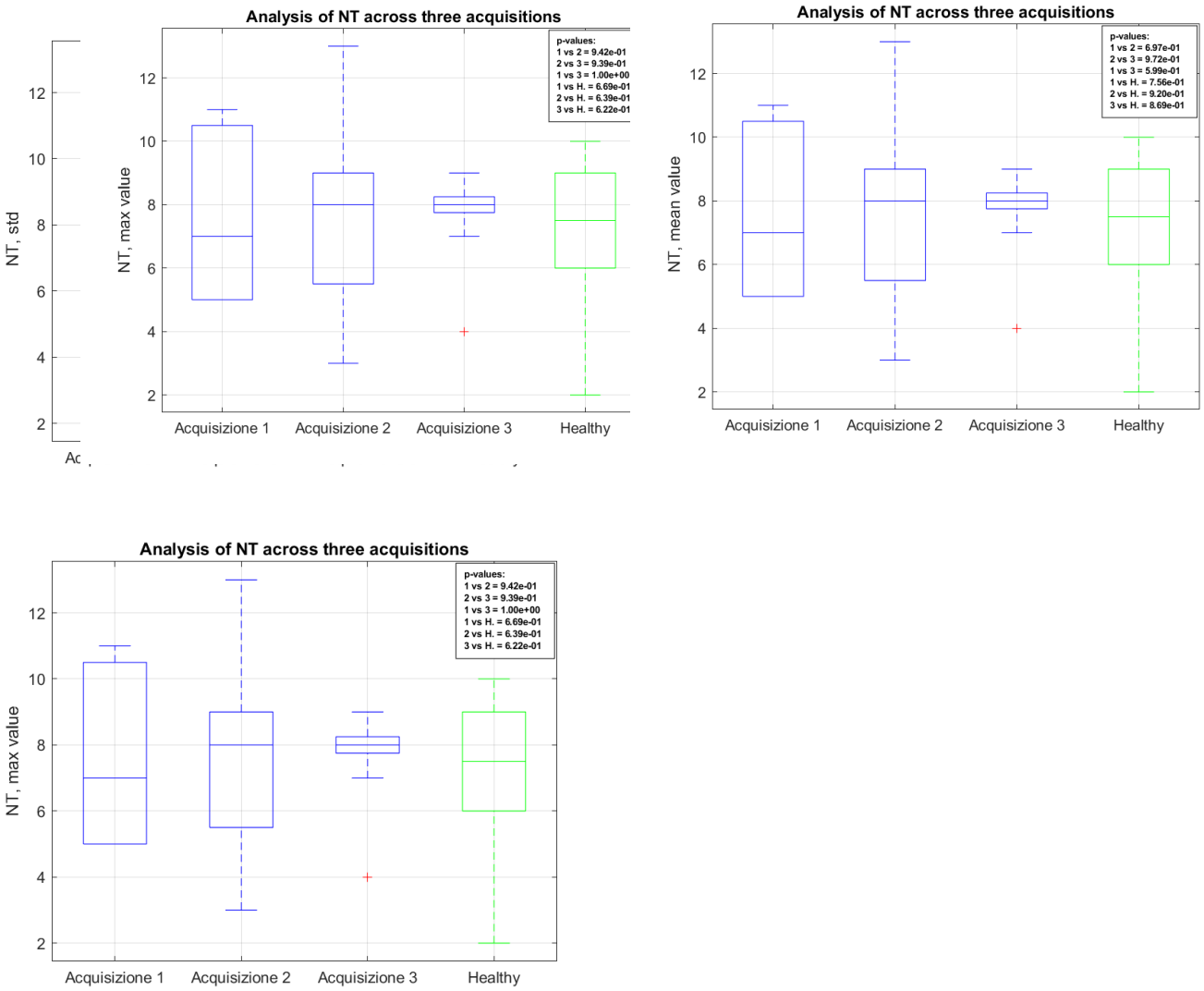

Figure 3.18: The three graphs represent the standard deviation, maximum value, and average value of number of trees for the entire dataset of lesion-related data across the first, second, and third acquisitions. The green boxplot indicate the corresponding parameter calculated for all acquisitions performed on healthy skin. In each graph, the p-value for comparisons between the first and second, second and third, first and third acquisitions, as well as between each acquisition and healthy skin, is shown in the top right corner.

- **Number of branches**

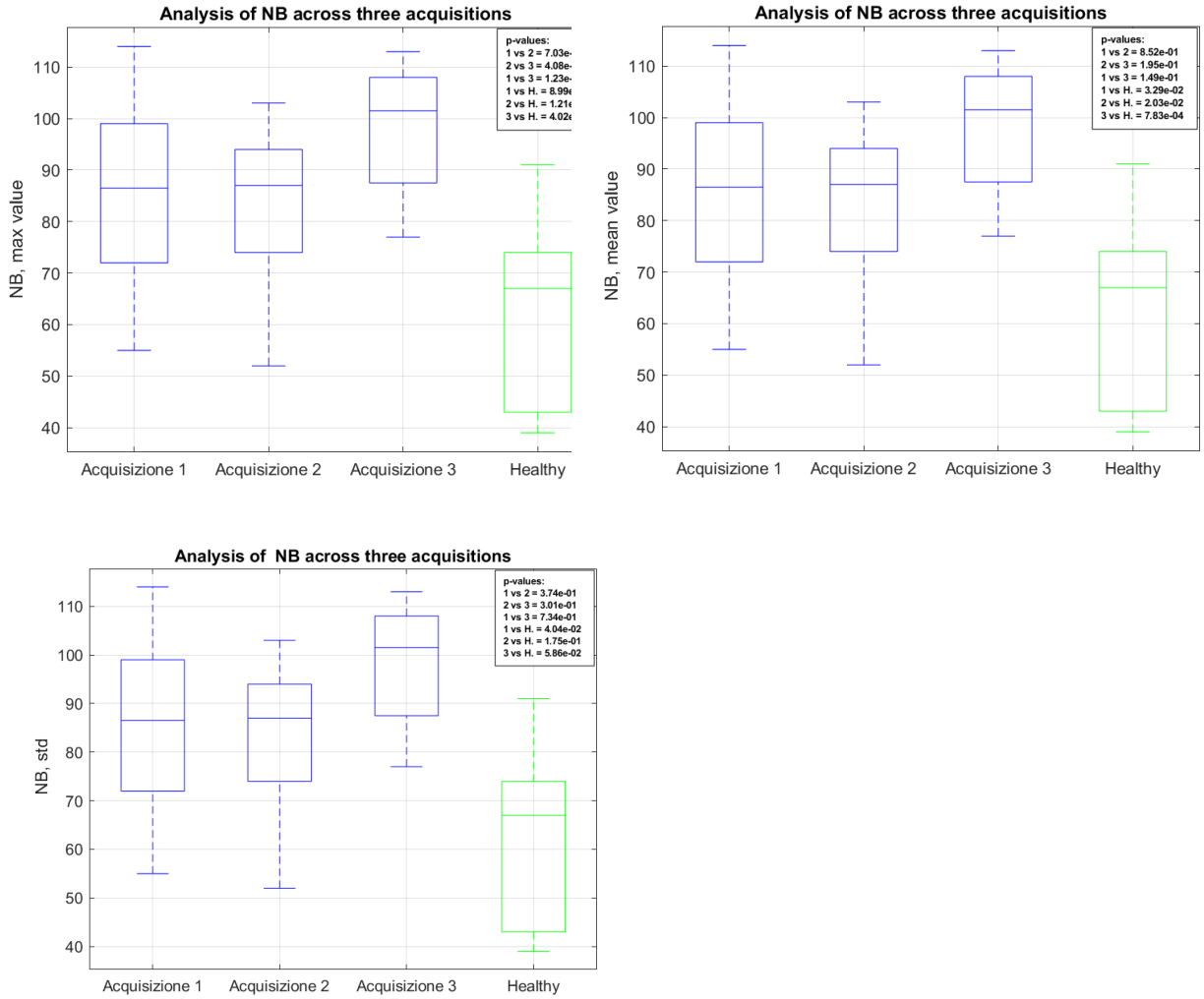

Figure 3.19: The three graphs represent the standard deviation, maximum value, and average value of number of branches for the entire dataset of lesion-related data across the first, second, and third acquisitions. The green boxplot indicate the corresponding parameter calculated for all acquisitions performed on healthy skin. In each graph, the p-value for comparisons between the first and second, second and third, first and third acquisitions, as well as between each acquisition and healthy skin, is shown in the top right corner.

4. Discussion

This section analyzes the results and their clinical relevance, focusing particularly on monitoring the effects of radiotherapy treatment through the quantitative analysis of vascular parameters. A comparison between lesion and healthy skin is also explored to assess differences in vascular parameters between the two conditions. This comparison provides valuable insights into the distinctive characteristics of lesions and their behavior realtive to healthy tissue.

However, it is important to consider several limitations. These include the potential influence of factors such as acquisition artifacts and inaccuracies in positioning between different sessions, which could affect or alter the vascular parameter results. Additionally, post-radiotherapy tissue inflammation may trigger immune responses that impact the analyzed parameters, potentially delaying the effects of treatment.

4.1 Healthy skin vs lesion

Several studies demonstrate the ability of OCT to highlight significant differences in vascular morphology between healthy skin and tumor lesions [20,24].

Healthy skin is characterized by a homogeneous vascular distribution, with a well-organized capillary network and microcirculation consisting of ascending arterioles, capillary loops, and venules. This superficial vascular system is primarily located in the capillary plexus of the dermal papilla, providing nourishment and oxygen to the epidermis and the superficial portion of the dermis. In normal conditions, blood vessels show uniform density and stable structure, with no signs of abnormalities.

When skin lesions are present, significant changes are observed in the microcirculation, influencing both the density and structure of blood vessels. In neoplastic lesions, these vascular alterations are particularly pronounced and complex. Tumor lesions exhibit a significantly higher vascular density compared to healthy skin, with blood vessels that not only supply nutrients to the growing tumor but also facilitate the hematogenous spread of tumor cells [20,24].

From a vascular structural perspective, skin lesions are often associated with larger caliber vessels, irregular distribution, and atypical branching. Specifically, many of these lesions show tortuous vessels, which can appear in the form of spirals or serpentine vessels. These

tortuous and disorganized vessels are a clear indicator of tumor angiogenesis, which can manifest even in the early stages of tumor development.

Angiogenesis is the process through which a tumor develops new blood vessels to meet its increasing metabolic and oxygen demands, surpassing simple nutrient diffusion when the tumor volume becomes significant. This process is not only an indicator of tumor progression but also a key feature distinguishing healthy skin from tumor lesions [21,23].

OCTA has proven to be an effective non-invasive tool for visualizing differences in skin vascularization. It allows us to observe changes in microcirculation, revealing increased vascular density, irregular distribution, and atypical branching in lesions, while healthy skin maintains regular vascular architecture.
This study reveals significant differences between lesions and healthy skin, as shown in Fig 3.12 An illustrative example is provided by the case of the first patient, where four lesions are compared to healthy skin. In this example, we observe statistically significant differences between the lesions and healthy skin, with the healthy skin showing lower values in vascular density, vessel radius, number of branches, and inflection count metric. The following images present box plots for a specific parameter for both lesions and healthy skin. The data shows a p-value less than 0.05, indicating a statistically significant difference between the two groups.

4.2 Dataset-based quantitative analysis

Analysis of the data collected at three time points ("pre-treatment," "post-treatment at 1 month," and "post-treatment at 3 months") reveals a complex picture that reflects the interaction between radiotherapy and vascular changes in skin lesions. The results indicate that radiotherapy induces significant changes in the microvascularization of the lesions. Previous studies suggest that the progression or regression of skin lesions can be monitored by studying parameters such as vascular density, tortuosity, and vessel morphology [23,24,42] . In general, a reduction in tumor volume should typically be associated with an improvement in vascular organization, with a reduction in tortuosity and a normalization of vascular density, approaching the configuration of healthy skin, as discussed in the previous section.

However, the results observed at post-treatment time points, particularly at 1 and 3 months, suggest a possibly immune response leading to an increase in vascular density and tortuosity. This process is generally due to the acute inflammatory response, which stimulates the formation of new blood vessels. The beneficial effects of radiotherapy, however, become apparent only after about 6 months, when tumor cells stop proliferating and undergo apoptosis.

Radiotherapy triggers a complex inflammatory response in both tumor and healthy tissues, which can lead to significant changes in vascularization. This process begins with the immediate release of damage-associated molecular patterns (DAMPs), signals released by damaged or dying cells following treatment. DAMPs are recognized by pattern recognition receptors (PRRs) present on immune cells such as macrophages and dendritic cells, activating a series of immune responses. Simultaneously, radiotherapy stimulates the production of reactive oxygen species (ROS), highly reactive molecules that can further damage already compromised cells. ROS, along with DAMPs, activate various transcription factors (such as NF-kB and AP-1) and cellular signaling pathways, promoting the production of pro-inflammatory cytokines. Among these are IL-1, IL-6, IL-12, IFN-α, IFN-β, and TNF-α, which are released at the site of damage. Pro-inflammatory cytokines play an important role in inducing an acute inflammatory response, favoring the activation of immune cells

such as T lymphocytes and macrophages, creating an environment that stimulates defense against the tumor.[43]

During the acute phase of the inflammatory response, increased vascular permeability facilitates the infiltration of immune cells and fluids into the site of injury. This process is mediated by pro-inflammatory cytokines and leads to vasodilation. At the same time, these cytokines stimulate the production of pro-angiogenic factors like VEGF, which promotes neoangiogenesis to restore blood supply to the damaged tissues. However, the emerging blood vessels often show an irregular organization, characterized by tortuosity and impaired functionality, leading to disorganized angiogenesis [24,43-44].

Considering the described inflammatory response and disorganized post-treatment neoangiogenesis, the results of our study highlight significant changes in the vascular parameters of the lesions.

Regarding vascular density (Fig 4.1) , both the maximum and average values showed a significant increase between the first and third acquisition, with an increase also observed between the second (1 month post-treatment) and third acquisition (3 months post-treatment). This result aligns with the acute inflammatory response following radiotherapy. The increase in vascular density reflects the neoangiogenesis driven by the formation of newblood vessels, a phenomenon that commonly occurs in the later phases post-treatment as part of the immune and regenerative response.

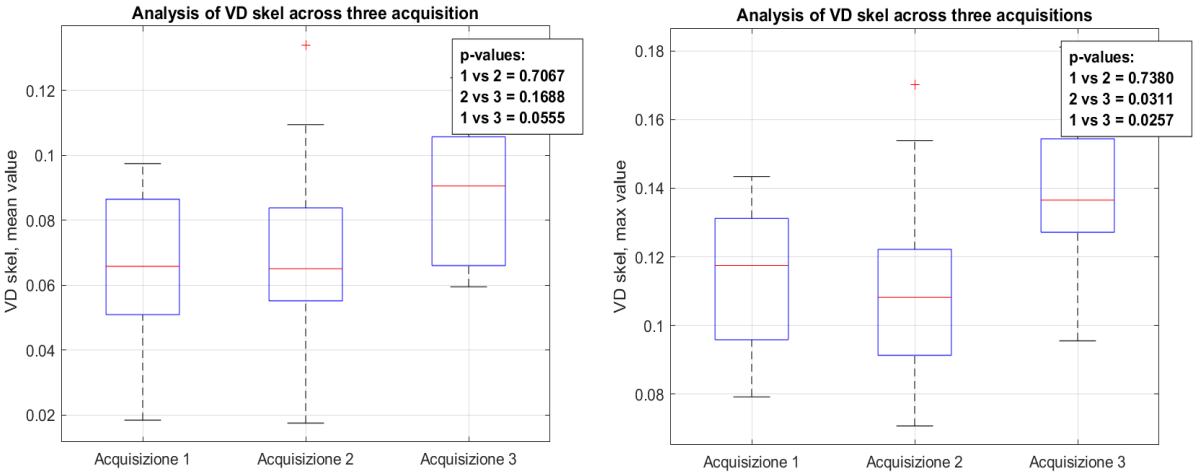

Figure 4.1: Graphs showing the average and maximum vascular density values across the three acquisitions , considering all lesion-related data. Statistical test results are reported at the top, comparing the first and second acquisitions, the second and third acquisitions , and the first and third acquisitions.

Concerning vessel radius (Fig 4.2) , significant decreases were observed between the second and third acquisition in both the average and maximum values. This may suggest that, while the initial response to treatment (at 1 month) leads to vasodilation and disorganized neoangiogenesis, a partial normalization of the vascular structure occurs over time. The increase in vascular density at 3 months might thus be accompanied by vessel reorganization, trending towards a more regular caliber, though still dysfunctional, in response to ongoing inflammation and tissue repair processes.

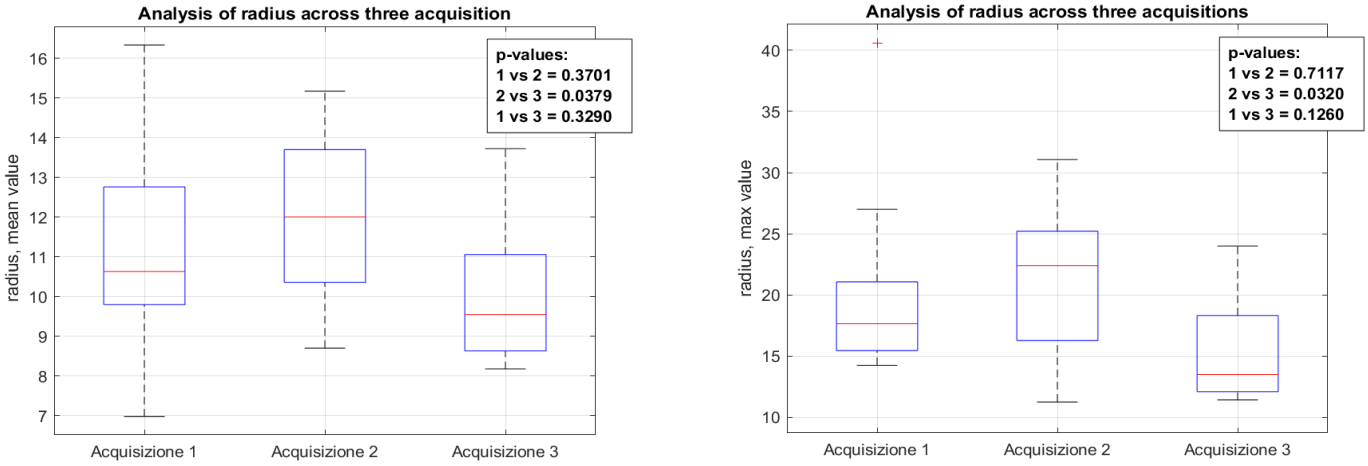

Figure 4.2: Graphs showing the average and maximum radius values across the three acquisitions , considering all lesion-related data. Statistical test results are reported at the top, comparing the first and second acquisitions, the second and third acquisitions , and the first and third acquisitions.

Regarding vascular tortuosity (Fig 4.3), the distance metric parameter showed a significant increase between the second and third acquisitions, as did the maximum value of the inflation count metric, which also rose notably during the same period. These changes suggest that vessel tortuosity increases in the post-treatment phase, reflecting disorganized angiogenesis, a hallmark of the acute inflammatory response that follows radiotherapy.

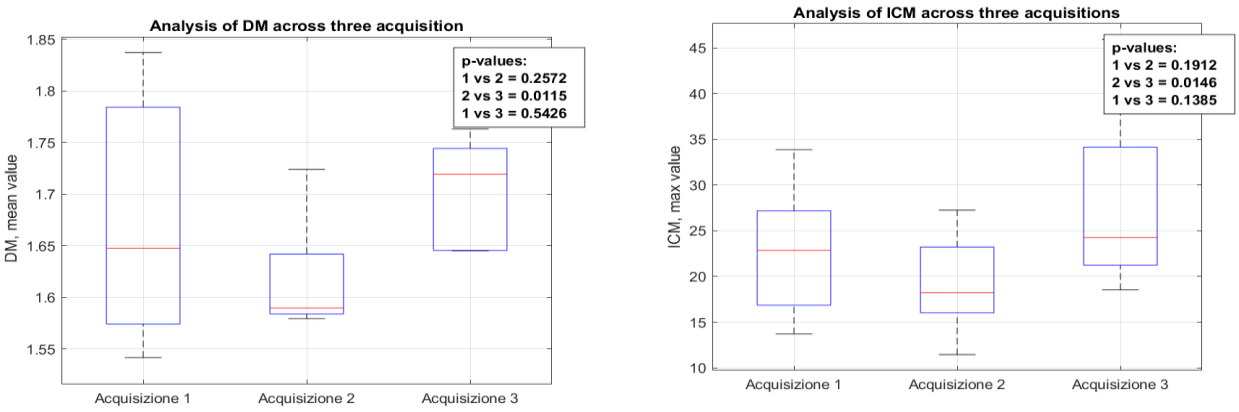

Figure 4.3: Graphs showing the average of distance metric and maximum of inflection count metric values across the three acquisitions , considering all lesion-related data. Statistical test results are reported at the top, comparing the first and second acquisitions, the second and third acquisitions , and the first and third acquisitions.

The number of branches showed a significant increase between the second and third acquisitions, as illustrated in Fig 4.4, aligning with the pattern of disorganized neoangiogenesis observed in the post-treatment period. Radiotherapy-induced angiogenesis not only leads to the formation of new blood vessels but also to greater branching, indicating an attempt to restore blood and oxygen supply to the damaged tissues.

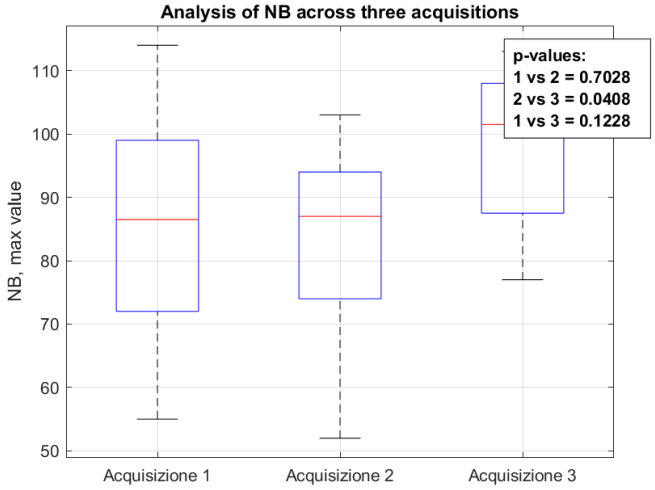

Figure 4.4: Graphs showing the average and maximum number of branches values across the three acquisitions , considering all lesion-related data. Statistical test results are reported at the top, comparing the first and second acquisitions, the second and third acquisitions , and the first and third acquisitions.

These parameters provide important insights into the vascular response and serve as indicators of how the tumor tissue is reacting to treatment, suggesting a complex dynamic of repair and regeneration.

4.3 Limitations

It is important to consider some limitations of this study that could influence the results and their interpretation. Specifically, the post-radiotherapy inflammatory response, which can persist for up to three months, may alter the vascular parameters analyzed, as discussed in previous sections. This inflammatory response could bias the effects of the treatment, making it difficult to draw definitive conclusions about lesion regression or progression after 3 months from the radiotherapy session.

Therefore, it is important to acknowledge that, due to this ongoing inflammatory response, we cannot definitively state whether the lesion is truly regressing or whether the treatment is producing an entirely positive or negative outcome. A potential solution to this limitation could be long-term observation beyond the three-month period, allowing for a clearer understanding of vascular changes and their impact on the tumor.

Another limitation pertains to the precision of the imaging acquisitions. Acquisition artifacts can occur when the imaging device is not in perfect contact with the skin, particularly in anatomically challenging areas encountered in this study, such as the ear or shoulder. These artifacts may affect vascular parameters and compromise the accuracy of the results. Additionally, during the different acquisition sessions (pre-treatment, one month post-treatment, and three months post-treatment), exact lesion positioning may not always be ensured. Such positioning inaccuracies could lead to variations in the observed vascular patterns, reducing the accuracy of comparisons among the three acquisitions and complicating the correct interpretation of vascular changes over time.

5. Conclusions and Future Developments

OCTA has proven to be an effective non-invasive device for monitoring the evolution of skin lesions over time, offering a promising prospect for the future. It could enable early observation of therapeutic progress in skin lesions, allowing treatment adjustments based on the response observed at an early stage. This approach could lead to more effective treatments, ultimately improving patient care.

Moreover, OCTA is advantageous because it's a non-invasive technique that doesn't require surgery or leave scars or ionizing radiations. The ability to analyze and monitor lesions without relying on invasive biopsies, which leave scars, makes OCTA particularly valuable in dermatology. A strength of this study is the importance of OCTA in distinguishing between healthy skin and lesions, a feature that could be exploited for diagnosing various skin conditions.

In its current technical form, OCTA is already a commercially available non-invasive morphological method in ophtalmology, and future advances are expected to expand its practical applications and clinical indications in dermatology [20] .

This study is significant as it represents the first non-invasive longitudinal monitoring of pre-cancerous and cancerous skin lesions, offering valuable insights into their evolution over time. By enabling continuous assessment,this approach could pave the way for future studies and clinical practices , where ongoing monitoring plays a key role in refining treatment strategies.

The analysis of OCTA images allowed us to draw conclusions on the effects of radiotherapy on superficial skin lesions at three distinct time points: before radiotherapy, one month after, and three months post-treatment. Significant variations in vascular network parameters were observed over time, and these changes were correlated with the effects on skin tissue. These findings provide valuable insights into the impact of radiotherapy on pre-cancerous and cancerous skin lesions and may help guide future therapeutic strategies.

Specifically, it was found that, although the lesions evolved and significant differences were observed between imaging sessions, the inflammatory response during the first three months after treatment had a significant impact on vascular parameters, complicating the assessment of the overall assessment of treatment response. However, extending the study beyond the three-month period could provide a clearer understanding of vascular changes and their

influence on tumor response, offering a more precise evaluation of long-term therapeutic outcomes.

Monitoring skin inflammation is particularly useful for clinicians, as each patient reacts differently to therapy. While a definitive assessment of radiotherapy success might typically take six months, OCTA can be helpful in detecting the first vascular changes or inflammatory responses to radiotherapy well before this time. The ability of OCTA to provide insights into therapy response highlights its potential to contribute significantly to dermatological and oncological care.

Bibliography

[1] Konukman, Ferman. (2019). The Effects of Multimedia Computer Assisted Instruction (CAI) on Teaching Tennis in Physical Education Teacher Education.

[2] Fore J. A review of skin and the effects of aging on skin structure and function. Ostomy Wound Manage. 2006 Sep;52(9):24-35; quiz 36-7. PMID: 16980727

[3] Linares MA, Zakaria A, Nizran P. Skin Cancer. Prim Care. 2015 Dec;42(4):645-59. doi: 10.1016/j.pop.2015.07.006. PMID: 26612377.

[4] Dildar, M.; Akram, S.; Irfan, M.; Khan, H.U.; Ramzan, M.; Mahmood, A.R.; Alsaiari, S.A.; Saeed, A.H.M; Alraddadi, M.O.; Mahnashi, M.H. Skin Cancer Detection: A Review Using Deep Learning Techniques. Int. J. Environ. Res. Public Health 2021, 18, 5479. https:// doi.org/10.3390/ijerph18105479

[5] Simões MCF, Sousa JJS, Pais AACC. Skin cancer and new treatment perspectives: a review. Cancer Lett. 2015 Feb 1;357(1):8-42. doi: 10.1016/j.canlet.2014.11.001. Epub 2014 Nov 11. PMID: 25444899.

[6] McDaniel B, Badri T, Steele RB. Basal Cell Carcinoma. 2024 Mar 13. In: StatPearls [Internet]. Treasure Island (FL): StatPearls Publishing; 2024 Jan–. PMID: 29494046.

[7] Gordon R. Skin cancer: an overview of epidemiology and risk factors. Semin Oncol Nurs. 2013 Aug;29(3):160-9. doi: 10.1016/j.soncn.2013.06.002. PMID: 23958214.

[8] Garcia-Zuazaga J, Olbricht SM. Cutaneous squamous cell carcinoma. Adv Dermatol. 2008;24:33-57. doi: 10.1016/j.yadr.2008.09.007. PMID: 19256304.

[9] Waldman A, Schmults C. Cutaneous Squamous Cell Carcinoma. Hematol Oncol Clin North Am. 2019 Feb;33(1):1-12. doi: 10.1016/j.hoc.2018.08.001. PMID: 30497667

[10] Que SKT, Zwald FO, Schmults CD. Cutaneous squamous cell carcinoma: Incidence, risk factors, diagnosis, and staging. J Am Acad Dermatol. 2018 Feb;78(2):237-247. doi: 10.1016/j.jaad.2017.08.059. PMID: 29332704.

[11] European consensus-based interdisciplinary guideline for invasive cutaneous squamous cell carcinoma. Part 1: Diagnostics and prevention–Update 202*3* Stratigos, Alexander J. et al. European Journal of Cancer, Volume 193, 113251

[12] Hasan N, Nadaf A, Imran M, Jiba U, Sheikh A, Almalki WH, Almujri SS, Mohammed YH, Kesharwani P, Ahmad FJ. Skin cancer: understanding the journey of transformation from conventional to advanced treatment approaches. Mol Cancer. 2023 Oct 6;22(1):168. doi: 10.1186/s12943-023-01854-3. PMID: 37803407; PMCID: PMC10559482

[13] Ferrante di Ruffano L, Dinnes J, Deeks JJ, Chuchu N, Bayliss SE, Davenport C, Takwoingi Y, Godfrey K, O'Sullivan C, Matin RN, Tehrani H, Williams HC; Cochrane Skin Cancer Diagnostic Test Accuracy Group. Optical coherence tomography for diagnosing skin

cancer in adults. Cochrane Database Syst Rev. 2018 Dec 4;12(12):CD013189. doi: 10.1002/14651858.CD013189. PMID: 30521690; PMCID: PMC6516952.

[14] Strojan P. Role of radiotherapy in melanoma management. Radiol Oncol. 2010 Mar;44(1):1-12. doi: 10.2478/v10019-010-0008-x. Epub 2010 Mar 18. PMID: 22933884; PMCID: PMC3423668.

[15] Hennequin C, Rio E, Mahé MA. Radiothérapie des cancers cutanés [Radiotherapy of skin cancers]. Cancer Radiother. 2016 Sep;20 Suppl:S249-55. French. doi: 10.1016/j.canrad.2016.07.026. Epub 2016 Aug 10. PMID: 27522189.

[16] Veness M, Richards S. Role of modern radiotherapy in treating skin cancer. Australas J Dermatol. 2003 Aug;44(3):159-66; quiz 167-8. doi: 10.1046/j.1440-0960.2003.06711.x. PMID: 12869039.

[17] Benkhaled S, Van Gestel D, Gomes da Silveira Cauduro C, Palumbo S, Del Marmol V, Desmet A. The State of the Art of Radiotherapy for Non-melanoma Skin Cancer: A Review of the Literature. Front Med (Lausanne). 2022 Jun 27;9:913269. doi: 10.3389/fmed.2022.913269. PMID: 35833108; PMCID: PMC9272768.

[18] Rong Y, Zuo L, Shang L, Bazan JG. Radiotherapy treatment for nonmelanoma skin cancer. Expert Rev Anticancer Ther. 2015;15(7):765-76. doi: 10.1586/14737140.2015.1042865. Epub 2015 May 8. PMID: 25955383.

[19] Pashazadeh A, Boese A, Friebe M. Radiation therapy techniques in the treatment of skin cancer: an overview of the current status and outlook. J Dermatolog Treat. 2019 Dec;30(8):831-839. doi: 10.1080/09546634.2019.1573310. Epub 2019 Mar 1. PMID: 30703334.

[20] Spaide RF, Fujimoto JG, Waheed NK, Sadda SR, Staurenghi G. Optical coherence tomography angiography. Prog Retin Eye Res. 2018 May;64:1-55. doi: 10.1016/j.preteyeres.2017.11.003. Epub 2017 Dec 8. PMID: 29229445; PMCID: PMC6404988.

[21] Detmar M. Tumor angiogenesis. J Investig Dermatol Symp Proc. 2000 Dec;5(1):20-3. doi: 10.1046/j.1087-0024.2000.00003.x. PMID: 11147670.

[22] Kaur G, Roy B. Decoding Tumor Angiogenesis for Therapeutic Advancements: Mechanistic Insights. Biomedicines. 2024 Apr 9;12(4):827. doi: 10.3390/biomedicines12040827. PMID: 38672182; PMCID: PMC11048662.

[23] Kreusch JF. Vascular patterns in skin tumors. Clin Dermatol. 2002 May-Jun;20(3):248-54. doi: 10.1016/s0738-081x(02)00227-4. PMID: 12074860.

[24] Deegan AJ, Talebi-Liasi F, Song S, Li Y, Xu J, Men S, Shinohara MM, Flowers ME, Lee SJ, Wang RK. Optical coherence tomography angiography of normal skin and inflammatory dermatologic conditions. Lasers Surg Med. 2018 Mar;50(3):183-193. doi: 10.1002/lsm.22788. Epub 2018 Jan 22. PMID: 29356051; PMCID: PMC5867274.

[25] Enaholo ES, Musa MJ, Zeppieri M. Optical Coherence Tomography. 2024 Oct 6. In: StatPearls [Internet]. Treasure Island (FL): StatPearls Publishing; 2024 Jan–. PMID: 39163419.

[26] Bille JF, editor. High Resolution Imaging in Microscopy and Ophthalmology: New Frontiers in Biomedical Optics [Internet]. Cham (CH): Springer; 2019. PMID: 32091677.

[27] Drexler W, Liu M, Kumar A, Kamali T, Unterhuber A, Leitgeb RA. Optical coherence tomography today: speed, contrast, and multimodality. J Biomed Opt. 2014;19(7):071412. doi: 10.1117/1.JBO.19.7.071412. PMID: 25079820.

[28] Fang Wei, Bin Lu, Jian Wang, Dan Xu, Zhengqing Pan, Dijun Chen, Haiwen Cai, and Ronghui Qu, "Precision and broadband frequency swept laser source based on high-order modulation-sideband injection-locking," Opt. Express 23, 4970-4980 (2015)

[29] Bouma BE, de Boer JF, Huang D, Jang IK, Yonetsu T, Leggett CL, Leitgeb R, Sampson DD, Suter M, Vakoc B, Villiger M, Wojtkowski M. Optical coherence tomography. Nat Rev Methods Primers. 2022;2:79. doi: 10.1038/s43586-022-00162-2. Epub 2022 Oct 13. PMID: 36751306; PMCID: PMC9901537.

[30] Welzel J. Optical coherence tomography in dermatology: a review. Skin Res Technol. 2001 Feb;7(1):1-9. doi: 10.1034/j.1600-0846.2001.007001001.x. PMID: 11301634.

[31] Ulrich M, Themstrup L, de Carvalho N, Manfredi M, Grana C, Ciardo S, Kästle R, Holmes J, Whitehead R, Jemec GB, Pellacani G, Welzel J. Dynamic Optical Coherence Tomography in Dermatology. Dermatology. 2016;232(3):298-311. doi: 10.1159/000444706. Epub 2016 Apr 23. PMID: 27104356.

[32] Furuya M, Nishiyama M, Kasuya Y, Kimura S, Ishikura H. Pathophysiology of tumor neovascularization. Vasc Health Risk Manag. 2005;1(4):277-90. doi: 10.2147/vhrm.2005.1.4.277. PMID: 17315600; PMCID: PMC1993966.

[33] Choi WJ, Paulson B, Yu S, Wang RK, Kim JK. Mean-Subtraction Method for De-shadowing of Tail Artifacts in Cerebral OCTA Images: A Proof of Concept. Materials (Basel). 2020 Apr 26;13(9):2024. doi: 10.3390/ma13092024. PMID: 32357466; PMCID: PMC7254351.

[34]] N. Otsu, "A Threshold Selection Method from Gray-Level Histograms," in IEEE Transactions on Systems, Man, and Cybernetics, vol. 9, no. 1, pp. 62-66, Jan. 1979, doi: 10.1109/TSMC.1979.4310076.

[35] Binotti WW, Saukkonen D, Seyed-Razavi Y, Jamali A, Hamrah P. Automated Image Threshold Method Comparison for Conjunctival Vessel Quantification on Optical Coherence Tomography Angiography. Transl Vis Sci Technol. 2022 Jul 8;11(7):15. doi: 10.1167/tvst.11.7.15. PMID: 35857329; PMCID: PMC9315074.

[36] Rahimi M, Khameneh EA, Riazi-Esfahani H, Mahmoudi T, Khalili Pour E, Kafieh R. Application of ImageJ in Optical Coherence Tomography Angiography (OCT-A): A Literature Review. J Ophthalmol. 2023 Nov 22;2023:9479183. doi: 10.1155/2023/9479183. PMID: 38033422; PMCID: PMC10686712.

[37] Gu, J.; Liao, J.; Zhang, T.; Zhang, Y.; Huang, Z.; Li, C. Quantitative Optimization of Handheld Probe External Pressure on Dermatological Microvasculature Using Optical Coherence Tomography-Based Angiography. *Micromachines* **2024**, *15*, 1128

[38] Gruionu G, Baish J, McMahon S, Blauvelt D, Gruionu LG, Lenco MO, Vakoc BJ, Padera TP, Munn LL. Experimental and theoretical model of microvascular network remodeling and blood flow redistribution following minimally invasive microvessel laser ablation. Sci Rep. 2024 Apr 16;14(1):8767. doi: 10.1038/s41598-024-59296-w. PMID: 38627467; PMCID: PMC11021487.

[39] Cheeseman, A.K.; Vrscay, E.R. Estimating the Fractal Dimensions of Vascular Networks and Other Branching Structures: Some Words of Caution. Mathematics 2022, 10, 839. https://doi.org/ 10.3390/math10050839.

[40] Bullitt E, Gerig G, Pizer SM, Lin W, Aylward SR. Measuring tortuosity of the intracerebral vasculature from MRA images. IEEE Trans Med Imaging. 2003 Sep;22(9):1163-71. doi: 10.1109/TMI.2003.816964. PMID: 12956271; PMCID: PMC2430603.

[41] Ágg B, Szilveszter B, Daradics N, Benke K, Stengl R, Kolossváry M, Pólos M, Radovits T, Ferdinandy P, Merkely B, Maurovich-Horvat P, Szabolcs Z. Increased visceral arterial tortuosity in Marfan syndrome. Orphanet J Rare Dis. 2020 Apr 15;15(1):91. doi: 10.1186/s13023-020-01369-w. PMID: 32293489; PMCID: PMC7160945.

[42] Braun RP, Rabinovitz H, Tzu JE, Marghoob AA. Dermoscopy research--an update. Semin Cutan Med Surg. 2009 Sep;28(3):165-71. doi: 10.1016/j.sder.2009.07.001. PMID: 19782940.

[43] Liu ZL, Chen HH, Zheng LL, Sun LP, Shi L. Angiogenic signaling pathways and anti-angiogenic therapy for cancer. Signal Transduct Target Ther. 2023 May 11;8(1):198. doi: 10.1038/s41392-023-01460-1. PMID: 37169756; PMCID: PMC10175505.

[44] Guipaud O, Jaillet C, Clément-Colmou K, François A, Supiot S, Milliat F. The importance of the vascular endothelial barrier in the immune-inflammatory response induced by radiotherapy. Br J Radiol. 2018 Sep;91(1089):20170762. doi: 10.1259/bjr.20170762. Epub 2018 Apr 20. PMID: 29630386; PMCID: PMC6223160.